



Analysis of the rheology of magnetic bidisperse suspensions in the regime of discontinuous shear thickening

Georges Bossis¹ · Alain Cifre¹ · Yan Grasselli^{1,2} · Olga Volkova¹

Received: 31 August 2022 / Revised: 4 January 2023 / Accepted: 3 February 2023 / Published online: 23 February 2023
© The Author(s), under exclusive licence to Springer-Verlag GmbH Germany, part of Springer Nature 2023

Abstract

The phenomenon of discontinuous shear thickening (DST) is observed in suspensions of solid particles with a very high-volume fraction. For suspensions of ferromagnetic particles, this transition can also be triggered by the application of a magnetic field as discussed by Bossis et al. (2016). Here, we explore the rheological behavior of a bidisperse suspension made of magnetic-carbonyl iron (CI) and non-magnetic-calcium carbonate (CC) particles with a brush-like coating of the same superplasticizer molecule. We highlight the synergetic effect of non-magnetic particles whose inclusion in the percolated frictional network amplifies the effect of the magnetic field on the remaining fraction of magnetic particles. In plate-plate geometry, a small fraction of ferromagnetic particles (about 5%) is sufficient to trigger the transition by the application of a magnetic field and optimum for the increase of viscosity. The progressive interpenetration of the coating layers of polymer and the demagnetizing field can explain this behavior.

Keywords Discontinuous shear thickening · Rheology · Magnetorheology · Bidisperse suspensions

Introduction

Magnetorheological (MR) suspensions are usually made of magnetic particles presenting a high saturation magnetization and a low hysteresis in the curve $M(H)$ where M is the magnetization and H the magnetic field. Particles like carbonyl iron (CI) are good candidates with a magnetization saturation $\mu_0 M \sim 2$ T, and they are used in a very large number of formulations of MR fluids. In the presence of a high enough applied magnetic field, the particles are attracted against each other and form columnar aggregates whose resistance to an applied mechanical stress is characterized by the yield stress which can reach 100 kPa under an induction $B \sim 0.8$ T (Genç and Phulé 2002). Besides the technical difficulty to apply such a high field, the main problem encountered with these suspensions is the high

density of the CI particles ($\rho_{CI} \sim 7.7$ g/cm³). This high density creates in the absence of flow, a rapid sedimentation, and more seriously, an irreversible aggregation between the particles if the suspension remains unmixed during a long time. To prevent this aggregation either due to the pressure of the sedimented particles or to the magnetic pressure in the presence of the field, particles are coated with different molecules which provide a repulsive force either due to an ionic charge or to entropic forces which prevent polymer brushes to interpenetrate each other. A review of the different attempts to reduce sedimentation, still keeping a high yield stress, is summarized in some reviews (Ashtiani et al. 2015; Morillas and de Vicente 2020). For instance, oleic acid was currently used for iron particles in non-polar liquid (Van Ewijk et al. 1999) and also aluminum stearate or lecithin which is the best one with mineral oil (López-López et al. 2008). In polar solvents like water or mixture of ethylene glycol and water, polyelectrolytes are good surfactants. The density of the iron particles can be reduced by grafting a thick polymer shell on their surface—for instance polymethyl methacrylate PMMA but at the expense of a reduced yield stress (Cho et al. 2005; Choi et al. 2006) since the magnetic force between two iron particles decreases very quickly with the gap between the particles (Klingenberg and Zukoski

✉ Georges Bossis
bossis@unice.fr

¹ Université University Côte d'Azur, CNRS UMR 7010, Institute of Physics of Nice, Parc Valrose, 06108 Nice, France

² Université University Côte d'Azur SKEMA Business School, 60 Rue Dostoievski – CS30085, 06902 Sophia Antipolis, France

1990; Bossis et al. 2019). A way to overcome this problem of sedimentation is to use core–shell particles, but with the core made of polymer and the shell containing magnetic nanoparticles (Choi et al. 2005; Jun et al. 2005). Another way to stabilize the particles against sedimentation and aggregation is to use bidisperse suspensions, or more precisely to mix magnetic particles of diameter in the micron range to magnetic nanoparticles. The nanoparticles are Brownian and their random motion acts like a thermodynamic force which can be repulsive if their concentration is high enough to fill the gap between the large particles. On the other hand, if these nanoparticles are magnetic like in ferrofluids, they form a halo at the surface of the large magnetic particles due to the magnetic force between their permanent magnetic moment and the soft magnetic particles (López-López et al. 2010); this shell of nanoparticles prevents the aggregation of the larger particles and also slow down their sedimentation. This is true for bidisperse suspensions of magnetite particles (Viota et al. 2007, 2009) and of CI particles dispersed in a ferrofluid—also made of magnetite nanoparticles (Chaudhuri et al. 2005; López-López et al. 2006; Wereley et al. 2006; Burguera et al. 2008). Simulations of bidisperse systems of magnetic particles also show an increase of yield stress compared to monodisperse ones (Ekwebelam and See 2009; Wu et al. 2016) due to a stronger microstructure induced by the magnetic field. The same kind of behavior with a smaller sedimentation rate and a better re-dispersibility was observed with bidisperse suspensions of CI particles with magnetic nanorods (Chin et al. 2001; Ngatu and Wereley 2007) or with mixture of iron platelets of different sizes (Shah et al. 2013). More recently, bidisperse MR fluids made of CI and magnetite nanoparticles coated with graphite oxide and gelatine were also shown to present a higher yield stress than pure CI particles and a better re-dispersibility (Fu et al. 2018). Nevertheless, the stability of the ferrofluid itself is often difficult to maintain in the presence of the high shear rates occurring in the gaps between the CI particles, and it appears that the optimum of concentration of ferrofluid can vary a lot between 10 and 40% depending on the precise composition of the suspensions. Other kind of nanoparticles like, for instance, organic clay (Chae et al. 2015; Aruna et al. 2019; Roupec et al. 2021) or fumed silica (Iyengar and Foister 2002) can also be used to reduce sedimentation, but, being non-magnetic, the yield stress of these suspensions is also reduced compared to the one based on magnetite nanoparticles, and furthermore the zero field state has a higher yield stress and plastic viscosity.

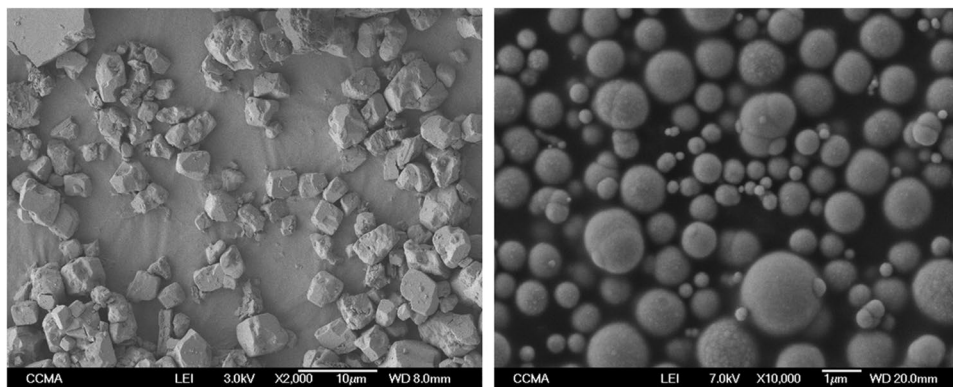
Another way to increase the performances of magnetorheological suspensions is to use the phenomenon of discontinuous shear thickening (DST) which is found in very concentrated suspensions of solid particles like polymer latex

(Laun et al. 1991), corn starch (Fall et al. 2010), silica or alumina (Franks et al. 2000), acicular calcium carbonate (Egres and Wagner 2005), and gypsum (Neuville et al. 2012).

Thanks to numerical simulations (Seto et al. 2013; Mari et al. 2014; Johnson et al. 2017; Singh et al. 2018; Guy et al. 2020), it is now well established that this transition, which appears as a sudden increase of the viscosity, is due to the abrupt onset of frictional contacts between the surfaces of the particles. These contacts appear when the hydrodynamic shear forces are strong enough to overcome the repulsive forces due to ionic layers in the case of polar solvents or to the adsorption or grafting of polymer layers at the surfaces of the particles.

By mixing a DST fluid made of fumed silica particles with CI particles, Zhang et al. (2008) have observed that they could keep the DST behavior at low volume fraction of CI particles. Nevertheless, the change of viscosity associated with the shear thickening was decreasing with the application of an external magnetic field. With a suspension of CI particles at a quite low volume fraction ($\Phi < 25\%$) in silicone oil (Tian et al. 2010; Jiang et al. 2015), a DST transition was observed with a large increase of the shear stress at a low shear rate (below 1 s^{-1}) by applying a large magnetic field ($B > 0.4$ Tesla) on the suspension. This was also the case for a suspension of CI particles containing sheets of graphite oxide, but the DST transition disappeared if the CI particles were coated with graphite oxide, showing the role of the friction on this transition (Chen et al. 2014). These previous works have shown that the application of a strong magnetic field could induce the DST transition in suspensions of magnetic particles. More recently, we have used with CI particles in ethylene glycol, a superplasticizer molecule used in cement industry which adsorbs on the surface of mineral particles through electrostatic interactions. This coating layer reduces the friction and allows to obtain high volume fraction (up to 68%), keeping a low yield stress. Above a certain critical shear rate, which depends strongly on the volume fraction of CI particles and can vary from 0.1 to a few hundred s^{-1} , we have a strong DST transition that we associate with the local expulsion of the coating molecules when the shearing stress overcomes a critical value. More interesting is the fact that this transition can be triggered with a low magnetic field and produces very high stresses (Bossis et al. 2016). For instance, it is possible to get a yield stress of more than 100 kPa with a field as low as 20 kA/m (Bossis et al. 2019). Still, there is always the problem with rapid sedimentation of CI particles having a density $\rho \sim 7.7 \text{ g/cm}^3$ and with the pressure exerted by the weight of sedimented particles which can end up with irreversible aggregation. A way to deal with this problem is to use mixtures of magnetic and non-magnetic particles whose average density would be much smaller than with a suspension of CI particles only. In this case, we could worry that adding a

Fig. 1 SEM image of CaCO₃ (CC) particles on the left side and carbonyl iron (CI) particles on the right side



part of non-magnetic particles will lower the field induced yield stress, but it is not the case: For the same volume fraction of CI particles, adding non-magnetic particles will, on the contrary, increase the field induced yield stress (Ulicny et al. 2010) although it is not always systematic (Pierce et al. 2022) (Cvek 2022). This result was obtained with volume fraction of 30% of CI particles and different volume fractions of hollow glass spheres. Numerical simulation show that non-magnetic particles participate to the construction of field induced aggregates, so the higher total volume fraction contributes to enhance the yield stress even if the added particles are not magnetic (Wilson and Klingenberg 2017).

Our aim here is to see if a mixture of magnetic and non-magnetic particles can show DST and to which extent the triggering of the DST by a magnetic field can be realized with a volume fraction of magnetic particles as low as possible. In a first section, we shall present the materials we are using for these experiments, namely, CI and CC particles. In a second section, we shall present the evolution of the DST transition for different fractions of CI particles at a given total volume fraction $\Phi = 0.705$ in the absence of a magnetic field, and we shall discuss the prediction of the homogenization model which considers the interstitial suspension between the large CC particles as a continuum. In the last section, we shall present the synergetic effect of the non-magnetic particles in the presence of a magnetic field and show that counterintuitively, it is maximum for a low fraction (~5%) of magnetic particles; we shall discuss this result with the help of the homogeneous model used in the interpretation of the viscosity of bidisperse suspensions.

Particles, suspensions, and suspension preparations

The particles we are using are made on one hand of carbonyl iron obtained from BASF (grade HQ) with a density $\rho = 7.7 \text{ g/cm}^3$ measured by gas pycnometer and, on the other

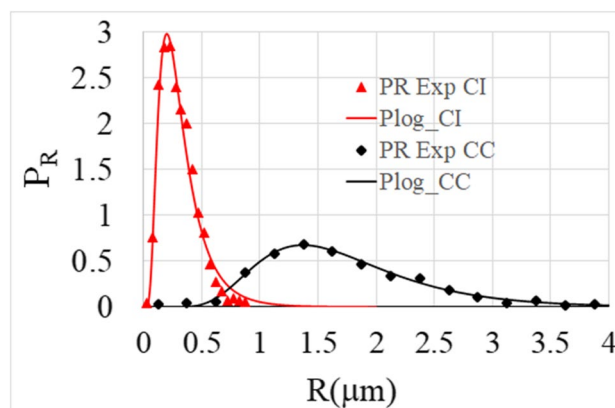


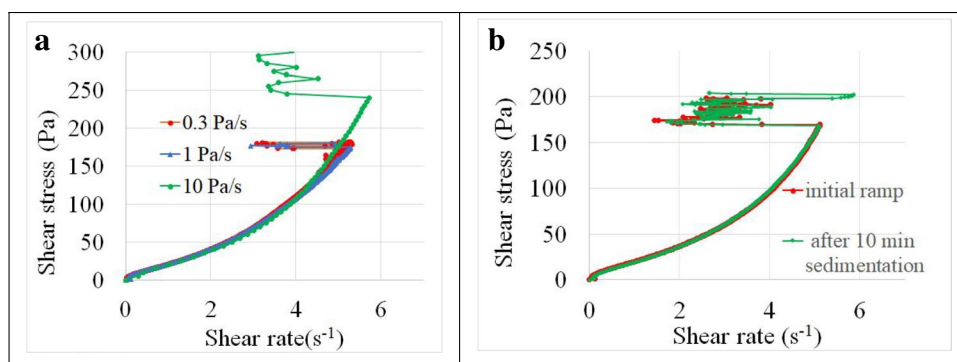
Fig. 2 Number density of probability versus the radius of the particles for CI particles (red symbols) and CC particles (black symbols). The solid lines are fits with a Lognormal distribution

hand, of calcium carbonate particles (BL200 from Chryso) of density 2.72 g/cm^3 . Their size distribution was obtained with the help of several SEM images analyzed with ImageJ with a total of 2300 particles for CI and 600 for CC particles. Typical images are shown in Fig. 1. We see that the iron particles are well spherical, whereas the CC particles have an irregular shape close to rhomboidal one, but they have approximately equal sizes in all directions: as proved by the analysis of their sphericity with ImageJ, the ratio of the large axis over the small one is only 1.2. The average radius and standard deviation calculated from the experimental data were $a_{CI} = 0.297 \text{ }\mu\text{m}$ and $\sigma_{\text{std-}CI} = 0.15 \text{ }\mu\text{m}$ and $a_{CC} = 1.75 \text{ }\mu\text{m}$ and $\sigma_{\text{std-}CC} = 0.809 \text{ }\mu\text{m}$.

The size distribution density is correctly represented by a Lognormal distribution:

$$P(R) = \frac{1}{R\sigma\sqrt{(2\pi)}} \exp\left[-\frac{(\ln R - \mu)^2}{2\sigma^2}\right] \tag{1}$$

Fig. 3 **a** Effect of the rate of rising stress for the three rates: 0.3, 1, and 10 Pa/s. Total volume fraction, $\Phi=0.705$; solid fraction of CaCO_3 , $F_{\text{CC}}=89\%$. **b** Effect of a rest of 10 mn after the first ramp of stress. $\Phi=0.705$; solid fraction of CaCO_3 ; $F_{\text{CC}}=89\%$



The fits of the two size distributions are represented in Fig. 2; the parameters of the fit were respectively $\mu=-1.292$ and $\sigma=0.575$ for CI particles and $\mu=-0.475$ and $\sigma=0.4027$ for CC particles. Even for iron particles, the Brownian force (kT/a_{CI}) remains negligible compared to the shear force $6\pi\eta\dot{\gamma}a^2$ in all experimental situations. The ratio of the shear force to the Brownian force is the Péclet number, and for instance, with a shear rate $\dot{\gamma} > 1 \text{ s}^{-1}$ and a viscosity $\eta > 1 \text{ Pa}\cdot\text{s}$, we have $\text{Pe} > 100$.

For both types of particles, we used the same superplasticizer molecule whose commercial name is Optima 100 made of a short polyethylene oxide (PEO) chain (in average 44 $\text{O}-\text{CH}_2\text{CH}_2$ groups) and a diphosphonate head with sodium counter ions. As in a preceding work where we have used it with calcium carbonate particles, we shall name it PPP44 (Bossis et al. 2017). It is the phosphonate head negatively charged which binds electrostatically with the positive charges of iron and CC surfaces (Morini 2013; Bossis et al. 2017). In all the suspensions, the mass of PPP44 used was 2 mg/g of solid corresponding to the beginning of the “plateau” of the adsorption isotherm for both particles (cf Annex B). The detailed balance of the interaction forces acting between particles in the presence of a superplasticizer is described in the reference Bossis et al. (2017). In this reference, it is shown that, for the same superplasticizer, the resulting force between two coated particles is always repulsive at rest. The suspending liquid was a mixture of polyethylene glycol and water with respective proportions 85% and 15%; this proportion corresponds to a minimum of evaporation of the mixture as obtained by recording the variation of mass with time of a sample for different ratios of water and polyethylene glycol.

After adding the components, the suspensions were stirred for 5 min using a vortex mixer, placed in an ultrasound bath for 5 min, and vortex-stirred again for 5 min. Then, the suspension was stored at 4 °C during about 12 h. Just before starting rheometric experiments the suspension was mixed again with the vortex and briefly degassed under vacuum to remove remaining bubbles.

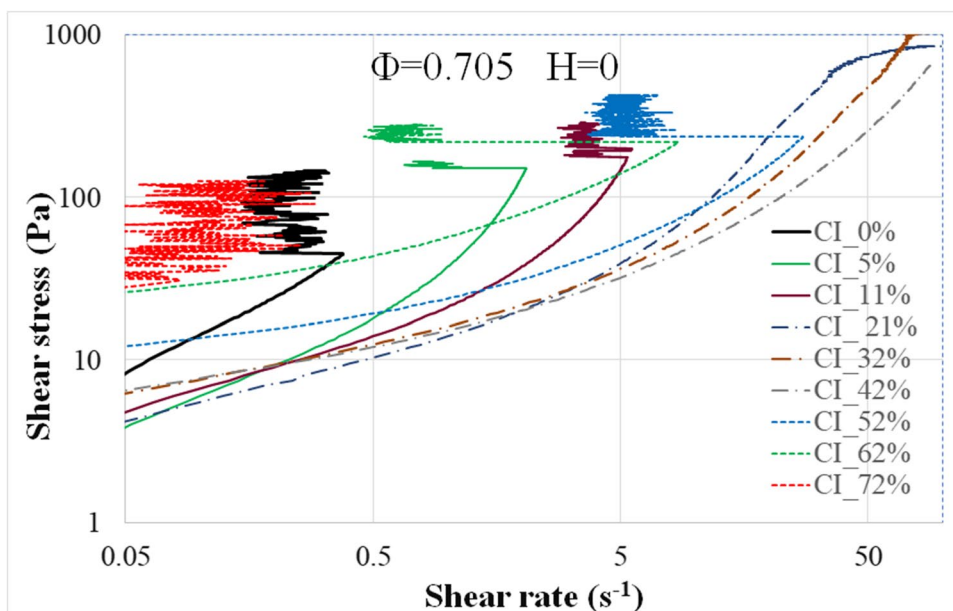
A pre-shear was realized on all experiments with a ramp of stress from 0 to typically 100 Pa which is below the critical one. It is then maintained constant during 3 mn and followed by a rest time of 30 s at zero stress. Then, a linear ramp of stress was applied at a rate of 0.5 or 1 Pa/s and with an acquisition rate of 1 or 2 points/s. As shown in Fig. 3a, where we have done three experiments at different rates of stress increase, this rate is slow enough to reach the equilibrium. Note that the effect of a fast increase (10 Pa/s) is mainly to delay the DST transition. For all the experiments, the temperature was $T=20 \text{ °C}$, and a solvent trap was used with the composition of 85% water and 15% polyethylene glycol already mentioned.

In concentrated suspensions, the positioning of the sample requires special care to allow the relaxation of the normal forces that are generated during the compression of the initial droplet. In the last step from 2 to 1 mm, the descent speed is regulated to a few micron/s with a typical rotating speed of 0.1 rpm, and we check that we end up with a negligible axial force on the upper plate.

Experimental results at zero magnetic field

We have used the plate-plate geometry with a gap of about 1 mm. The plate-plate geometry is interesting relatively to the sedimentation since, because of the small gap in the vertical direction, the redispersion of the sedimented particles is quickly obtained under a pre-shear of a few minutes. Actually, we did not observe any significant differences on the rheogram before the transition if we do a second stress ramp at a low enough rising rate (Fig. 3a at 0.3 Pa/s and 1 Pa/s) or also after a rest of 10 mn (Fig. 3b). Furthermore, even if an outward migration of particles was observed (Merhi et al. 2005) in torsional flow, it is a slow phenomenon which tends to disappear at high volume fraction (Kim et al. 2008). So, this plate-plate geometry is likely more adapted if we want to keep a homogeneous volume fraction and repartition of the two different kinds of particles. One problem related to this

Fig. 4 Total volume fraction $\Phi=0.705$ for different volume percentage F_{CI} of carbonyl iron. Raw curves in plate-plate geometry. The dotted lines are for fractions $F_{CI} \geq 50\%$; the dashed dotted lines are for fractions F_{CI} which do not present a DST transition



geometry is the fact that at high shear rates, the centrifugal forces become high enough to eject the suspension outside the gap between the plates; also above the jamming transition, the normal pressure generated by the motion of the aggregated network of particles can overcome the capillary pressure and produces granular lump of particles protruding outside the gap (Cates et al. 2005). The second well-known problem is the fact that the shear rate varies from zero at the center of the disk to its maximum $\dot{\gamma}=\Omega R/h$ on the rim where $r=R$. In the case of a Non Newtonian fluid where the stress is not just proportional to the shear rate, the relation between the stress and the shear rate must be corrected with the help of the Mooney-Rabinovitch equation: which relates the true yield stress, τ , to the stress, τ_N , given by the software for a Newtonian fluid:

$$\tau = \frac{\tau_N}{4} \left[3 + \frac{\dot{\gamma}}{\tau_N} \frac{d\tau_N}{d\dot{\gamma}} \right] \tag{2}$$

where $\tau_N(\dot{\gamma})$ is the curve given by the software of the rheometer based on a Newtonian fluid. On the contrary with the cylindrical Couette flow, we do not need to do this correction assuming that, due to the small gap, the shear rate can be considered to be equal to its mean value: $\dot{\gamma} = \Omega(R_e - R_i)/h$. The other advantage of the cylindrical Couette geometry is that the suspension cannot be expelled from the gap at high shear rates. On the other hand, the main disadvantage is that we can have a strong shear induced migration in the presence of a shear rate gradient. This migration was first observed by Nuclear Magnetic Resonance in concentric cylinders (Abbott et al. 1991; Graham et al. 1991; Chow et al. 1994), with monodisperse suspensions. With bidisperse suspensions, as the shear induced diffusion is proportional to $\dot{\gamma}a^2$ (Fall et al. 2010), we expect a stronger diffusion of the

bigger particles towards the zone of lower shear rate gradient (here the outer cylinder) and so a possible segregation of the particles depending on their sizes. The larger particles were observed to migrate towards the outer cylinder in bidisperse suspensions both experimentally (Graham et al. 1991) and by numerical simulation (Pesche et al. 1998; Shauly et al. 1998). In a wide gap cylindrical Couette cell (Fall et al. 2015), a large migration towards the outer cylinder was observed by magnetic resonance imaging on a polydisperse Cornstarch suspension at $\Phi=0.44$. Due to this possibility of differential migration, and although the use of Eq. (2) needs a careful smoothing or a fit by parts of the experimental curves, we have used plate-plate geometry in our experiments except when high shear rates were required.

In Fig. 4, we present the raw curves, stress versus shear rate, obtained at a total volume fraction $\Phi=0.705$ for different volume percentage of iron particles: $F_{CI}=V_{CI}/(V_{CC}+V_{CI})$. These curves are not corrected and are in a Log–Log scale. The dotted curves correspond to the fractions of iron larger or equal to 50%. The fractions $F_{CI}=21\%$, 32%, and 42% represented by the dash-dotted lines do not present a DST transition. This is due to that, in this range, the viscosity of the mixture is the lowest and, if there is a jamming transition, it is at a shear rate too high to be observed because the fluid is expelled before as we can see already in the upper part of these curves. On the other hand, we see that already at $F_{CI}=0.72$, the jamming transition takes place at a shear rate smaller than 0.1 s^{-1} , and it is very difficult to get a flowing mixture above $F_{CI}=0.72$. As already told, these rheograms obtained in plate-plate geometry should be corrected with the help of Eq. (2). In order to extract the main information from the corrected curve, we have fitted the upper part (stopping at the jamming stress) with a Herschel Buckley (HB) law, $\tau = \tau_{yHB} + K\dot{\gamma}^p$, and the lower part with a Bingham (B) law, $\tau = \tau_{yB} + \eta_B\dot{\gamma}$. The parameter p is the

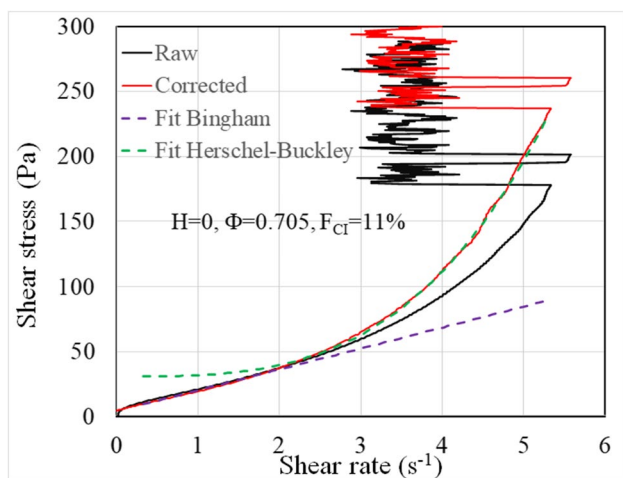


Fig. 5 The black curve is the raw one for $F_{CI}=0.11$. The solid red line is the corrected one given by Eq. (2). The green dashed line is the fit of the corrected curve with the Herschel Buckley law and the purple dashed line with the Bingham law

exponent of the HB law. All the values of the viscosity given in this paper except in Fig. 13a are the Bingham viscosity. We are using this Bingham viscosity instead of the apparent one $\sigma/\dot{\gamma}$ because we want to be able to identify a shear thickening behavior independently of the yield stress whose origin comes in residual adhesive forces between particles. The presence of shear thickening is associated to the formation of frictional contacts in the Wyart-Cates model, and the use of the apparent viscosity could hide a part of this shear thickening, if any, especially in the presence of a magnetic field.

An example of the corrected curve, in red, and of these two fits (dashed lines) is presented in Fig. 5. The upper part after the jamming point is just a shift of the initial curve by a quantity equal to the difference between the corrected critical stress and the initial one. The transition between the two fits takes place at the shear rate $\dot{\gamma}_t$ (here 2.2 s^{-1}). The values obtained for the two fits are recorded in the last six columns of Table 1 for all the volume fractions as well as the coordinates of the corrected DST transition point ($\dot{\gamma}_c, \sigma_c$).

The column σ_{c0} is the initial value of the DST critical stress before applying Eq. (2). We see that the corrected values are usually above the raw ones when the suspension is shear thickening, but it is the contrary at the highest volume fraction where the suspension is shear thinning. We shall discuss this point in more details in the next section. The value τ_{yHB} is just a fitting parameter without any physical meaning, whereas τ_{yB} is the dynamic yield stress, the stress needed to break continuously the aggregates in the regime of low shear rates, which is associated with η_B , the Bingham viscosity. At last, p , the exponent of the Herschel Buckley law, gives an indication of the importance of the shear thickening before the DST transition. Above the DST transition, we observe a kind of stick slip behavior which is due to the dynamic of adsorption/desorption of the polymer PPP44 on the surfaces of the particles and whose apparent amplitude depends strongly on the acquisition rate since its characteristic time is about 0.1 s (Bossis et al. 2022).

We have presented all the corrected curves at $\Phi=0.705$ in Fig. 6. Note that in the following, all the rheograms presented without indications are corrected with Eq. (2) if they are done in plate-plate geometry. The colors are the same than in Fig. 4, but we are now in linear coordinates which allows a better appreciation of the range of changes in the critical point for the same total volume fraction. We see for instance that the critical stress passes from 48 Pa for $F_{CI}=0\%$ (black curve in the insert) to 210 Pa for $F_{CI}=5\%$ (solid green curve) and 222 Pa for $F_{CI}=11\%$ (brown curve). If we believe that the critical stress depends only on a balance between the applied stress and the repulsive force between the particles, here mostly the CC particles coated with the superplasticizer molecule, it is difficult to understand why this repulsive force would be much stronger if we add a small quantity of small CI particles. It seems rather to be correlated with the strong decrease of the Bingham viscosity when F_{CI} increases (cf. Table 1), passing from 110 Pa.s for $F_{CI} 0\%$ to 17 Pa.s for $F_{CI}=11\%$. This behavior is still amplified for the coefficient K of the Herschel Buckley fit. It appears that the balance between the global applied stress and the repulsive force between two particles is not

Table 1 Parameters defining the corrected curves at $\Phi=0.705$

$\Phi=0.705$	$\dot{\gamma}_c$	σ_{c0}	σ_c	τ_{yB}	η_B	$\dot{\gamma}_t$	τ_{yHB}	K	p
0%CI	0.38	45.0	46.9	2.5	110	0.28	6.62	158.3	1.33
5% CI	2.07	150	218	2.17	30.6	0.63	18.4	17.8	3.30
11% CI	5.33	178	238	3.07	17.0	2.2	28.8	1.01	3.19
21% CI				7.6	7.1	6.5	9.38	2.41	1.56
32%CI				6.7	5.4	13	24.5	0.66	1.71
42%CI				8.43	3.95	18	48.8	0.115	1.95
52% CI	27.3	237	257	15.0	6.23	7.2	33	1.02	1.62
62% CI	8.59	220	217	28.4	20.9	2.1	38.2	13.7	1.19
72%CI	0.083	31.0	25.2	15.5	145	0.04	10.6	41.8	0.43

Fig. 6 Corrected rheograms; total volume fraction $\Phi=0.705$ for different volume fractions F_{CI} of CI particles. The insert is a zoom in the low shear rate zone. Same legend as in Fig. 4

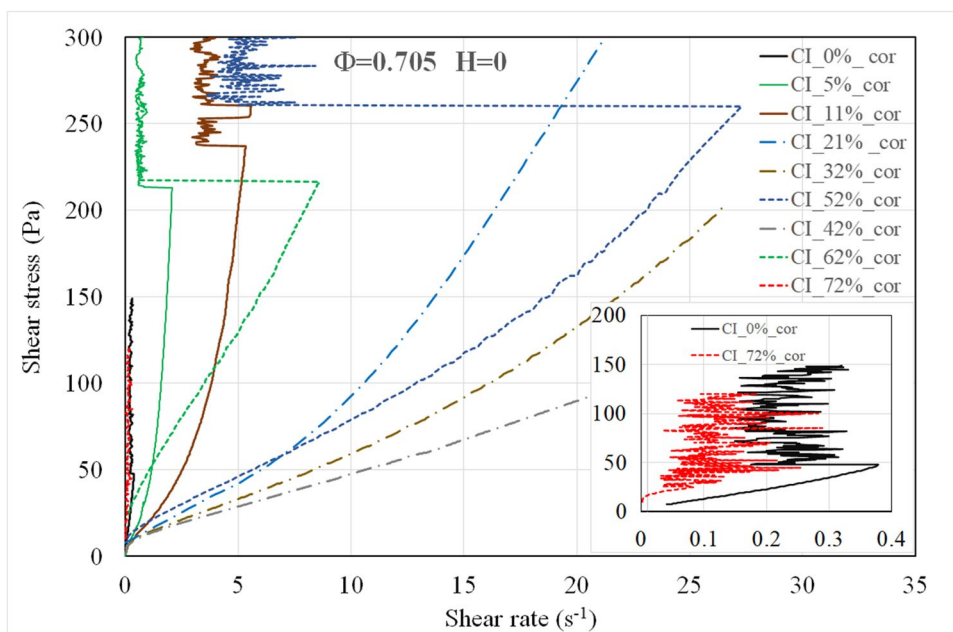
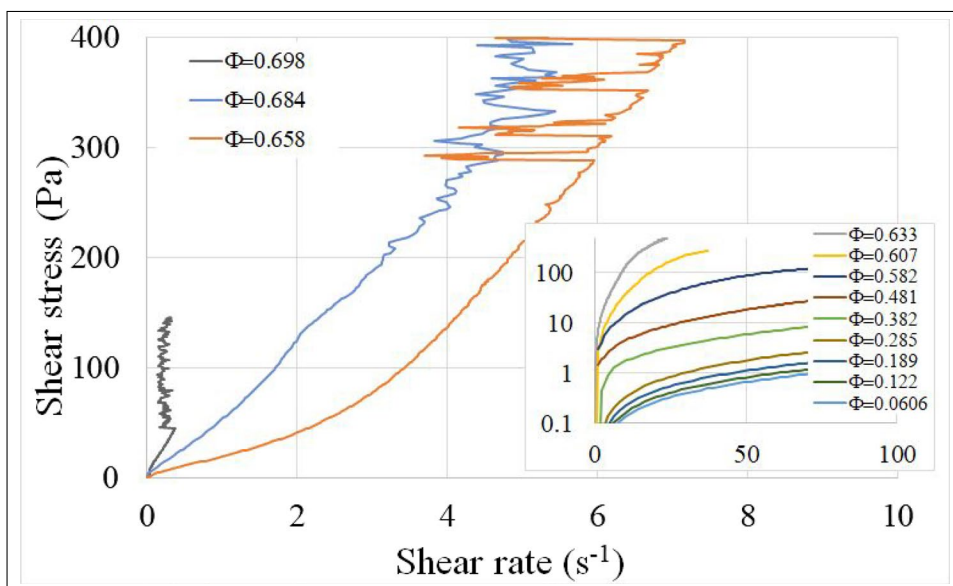


Fig. 7 Rheograms of pure CC suspension for different volume fractions



the only quantity which triggers the jamming transition. The mean gap between the large particles which will allow the propagation of the network of frictional contacts is likely also a key parameter which is also correlated to the viscosity. This mean gap tends to zero, and the viscosity diverges close to the maximum volume fraction for the pure CC suspension but adding a part of small particles and so removing CC particles for the same total volume fraction will increase the average gap between the CC particles. Even if locally some CC particles are pushed in frictional contact by a fluctuation in the local stress, this fluctuation will decrease quickly if the average gap between the particles is larger, allowing

to rearrange the structure and to dissipate this fluctuation, whereas it will propagate if the particles were already close to each other. It is interesting to note that the parameter p indicating the degree of shear thickening is very high at low volume fraction of iron like 5% or 11% but low at high volume fraction like 62% and even smaller than unity at 72%. It means that a low volume fraction of iron particles can contribute strongly to the formation of aggregates of CC particles when the shear rate is increased, but on the contrary, if the quantity of small particles dominates, the CC particles, when they are sheared, contribute to destroy the aggregates of small particles and produce a shear thinning behavior.

Table 2 Values of the volume fraction and viscosities entering in Eq. (7) for $\Phi = 0.65$

F_{CI}	$\eta(\Phi)$ $\Phi = 0.65$	Φ_{CC}	$\eta_r(\Phi_{CC})$	Φ'_{CI}	η'_{CI}	$\frac{\eta(\Phi)}{\eta_r \eta'_{CI}}$	Φ''_{CI} ($\Phi_{sh} = 0.52$)	$\frac{\eta(\Phi)}{\eta_r \eta'_{CI}}$
0.91	5.28	0.0605	1.15	0.628	2.73	1.67 ± 0.15	0.638	1.04
0.815	2.87	0.121	1.45	0.602	1.39	1.43 ± 0.13	0.62	0.93
0.720	2.04	0.182	1.91	0.572	0.66	1.62 ± 0.15	0.594	1.07

The two last columns correspond to the volume fraction of CI particles in a zone excluding the shell of lower volume fraction ($\Phi_s = 0.52$) around the CC particles

The rheograms corresponding to the suspension of pure CI particles ($F_{CI} = 1$) can be found elsewhere (Bossis et al. 2022); here, we have plotted in Fig. 7 the ones corresponding to the pure suspension of CC particles.

The rheograms are shear thickening at high volume fraction and then become quasi Newtonian from $\Phi = 0.58$ with a yield stress that is less than 1 Pa, so their Bingham viscosity at low shear rate was quite easy to define. Note that the DST transition is absent below $\Phi = 65.8\%$. The Bingham viscosity at low volume fraction, which will be used in Table 2, can be fitted for $\Phi < 0.3$ by $0.0115 + 0.0238\Phi + 0.1514\Phi^2 + 0.275\Phi^3$. In Figure 8a and b, we have plotted respectively the Bingham viscosity of the pure CC and of the pure CI suspensions versus the volume fraction. The error bars represent an uncertainty of 30% which reflects mainly the uncertainty on the choice of the range of shear rate for the Bingham fit at low shear rate. In the Wyart Cates model, the Bingham viscosity, η_B , is represented by the law:

$$\eta_B(\Phi) = A / \left(1 - \frac{\Phi}{\Phi_j^0} \right)^2 \quad (3)$$

where Φ_j^0 is called the jamming frictionless volume fraction. In this case, we obtain $A_{CC} = 0.13$ Pa.s and $\Phi_{j,CC}^0 = 0.721$ for the calcium carbonate particles. For the suspension of CI particles, the thickness of the polymer layer is not completely negligible compared to the radius of the particles. It can be approximated by the gyration radius of the polymer in a good solvent which is $d = b.P^{3/5}$ with $b = 0.526$ nm the

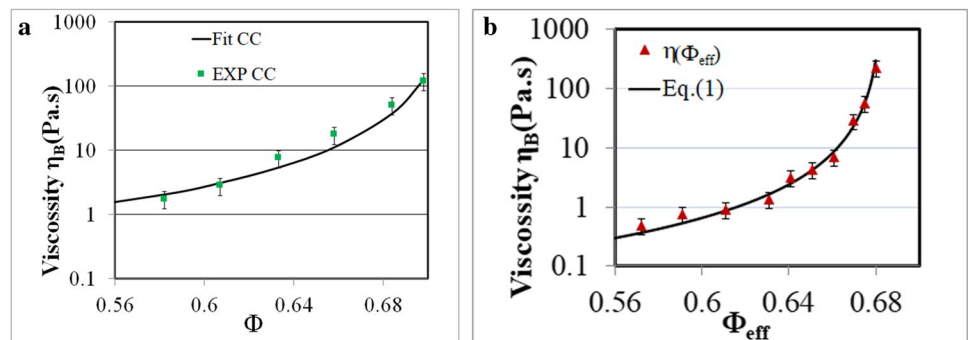
Kuhn length of the PEO group and $P = 44$ the number of monomers; we obtain $\delta = 5.1$ nm. The volume fraction Φ_{eff} is obtained from the third moment of the size distribution which is proportional to the volume of the solid, so taking $(a + \delta)^3$ instead of a^3 , we obtain for the effective volume fraction of the solid phase:

$$\Phi_{eff} = \frac{1}{1 + \frac{M_3(1-\Phi)}{M_{3\delta} \cdot \Phi}}$$

where $M_3 = 0.0642$ and $M_{3\delta} = 0.066$ are respectively the moments of the experimental distribution based on a^3 and $(a + \delta)^3$. We have then plotted the Bingham viscosity versus the effective volume fraction which takes into account the polymer thickness. The experimental curve is well represented by Eq. (3) with $\Phi_{j,CI}^0 = 0.684$ and $A_{CI} = 0.01$ Pa.s (cf. Figure 8b black solid line) instead of respectively 0.013 Pa.s and 0.678 if we do not consider the thickness of the polymer.

In Fig. 9a, we have plotted the Bingham viscosity of the bidisperse suspension versus the solid volume fraction of CI particles. As expected, it drops rapidly when a small fraction of iron particles replaces the CC particles since these smaller particles can occupy the voids between the large particles and be more or less considered a part of the suspending fluid. This is the approach of Chateau et al. (2008) that we shall develop in the next section. Another way to express this fact is to say that the maximum volume fraction of the mixture is higher than the one of the monodisperse suspension, thus explaining the

Fig. 8 **a** Bingham viscosity of a suspension of pure CC particles versus the volume fraction. The solid line is a fit by Eq. (3). **b** Bingham viscosity of a suspension of pure CI particles versus the effective volume fraction of CI particles. The black red line is a fit by Eq. (3)



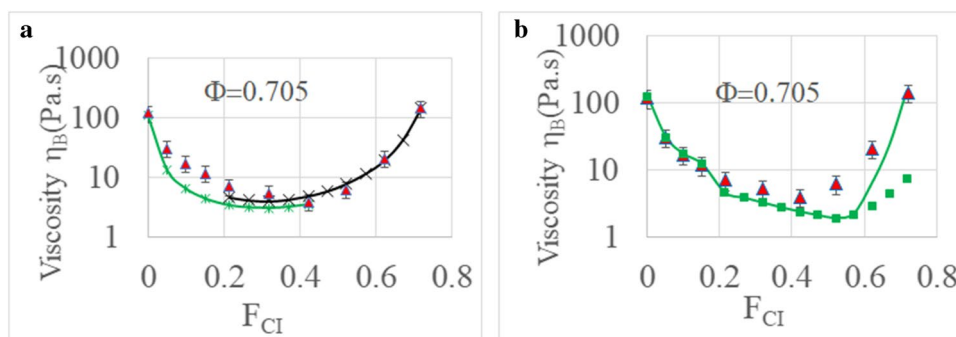


Fig. 9 a Bingham viscosity of a mixture CaCO₃/CI particles versus the solid volume fraction of CI particles. Red triangles: experiment; green line and black line from the maximum volume fraction of a mixture of bidisperse spheres obtained from simulation (Farr and

Groot 2009). **b** Bingham viscosity of a mixture CaCO₃/CI particles versus the solid volume fraction of CI particles. Red triangles, experiment (same points that in a); green squares, Eq. (7). Green line: with a shell of volume fraction $\Phi_s=0.563$.

decrease of the viscosity (Barnes et al. 1989; Pednekar et al. 2018). The study of the stacking of grains with different sizes and shapes has been the subject of numerous studies, in particular in the context of the formulation of concretes (De Larrard 1999). The change of the maximum packing fraction for bidisperse suspensions was studied for the same kind of particles. In this case, they are heuristic relations based on experimental data (Probstein et al. 1994; Shauly et al. 1998) and numerical simulations (Morris and Brady 1998; Farr and Groot 2009; Guy et al. 2020). In the case of bidisperse spheres, the maximum volume fraction for size ratios of the order of 5 is obtained for a proportion by volume of small spheres between 0.2 and 0.3 (Gondret and Petit 1997), (He and Ekere 2001), (Poslinski et al. 1988). Other models involve a loosening parameter expressing the dilation necessary to introduce a small particle into the space left between the large ones and another parameter to express the decrease in compactness near the wall of a large particle (Bournonville et al. 2004), (Vu et al. 2010). In our case, where the particles have different morphologies and are quite widely polydisperse, a sophisticated model whose parameters would remain arbitrary is useless. For a semi-quantitative approach, we will use the maximum volume fraction taken from the results of numerical simulation of a bidisperse suspension of spheres (Farr and Groot 2009). They gave data for several size ratios, in particular for 2, 3.3, and 5, allowing an extrapolation to our ratio: $\langle R_{moy-CC} \rangle / \langle R_{moy-CI} \rangle = 5.8$. Then, we approximate the maximum volume fraction Φ_0 versus F_{CI} in the following way. Firstly we take into account that, for the pure suspension of CC particles, the maximum volume fraction is not $\Phi_{RCP} = 0.643$ (the value obtained by Farr et al. for monodisperse spheres) but in our case 0.721, so for a given fraction F_{CI} of iron particles, we write $\Phi_j^0(F_{CI}) = (0.721/0.643) \Phi_{j, simu}^0(F_{CI})$ where $\Phi_{j, simu}^0(F_{CI})$ is the value extrapolated for a ratio of 5.8 of the diameters. The values of $\Phi_{j, simu}^0(F_{CI})$ were interpolated for different solid volume fraction by a polynomial fit; we obtain $\Phi_j^0(F_{CI} < 0.35) = 1.201F_{CI}^3 - 2.294F_{CI}^2 + 1.095F_{CI} + 0.722$

For larger values of F_{CI} , this approach cannot work since we have $\Phi_{j, CI}^0 \neq \Phi_{j, CC}^0$. So for values of F_{CI} larger than 0.35, we start from the pure iron suspension and write $\Phi_j^0(F_{CI}) = (0.684/0.643) \Phi_{j, simu}^0(F_{CI})$, and we obtain for the polynomial fit: $\Phi_j^0(F_{CI} > 0.35) = 1.029F_{CI}^3 - 1.972F_{CI}^2 + 0.944F_{CI} + 0.687$. Then, we use Eq. (3) with Φ_j^{0o} determined as described above and the parameter A adjusted to give either the viscosity for $F_{CI} = 0$ ($A = 0.121$ Pa.s; green line of Fig. 9a) or the last point at $F_{CI} = 0.72$ ($A = 0.082$ Pa.s; black line of Fig. 9a). We see that this approach reasonably well reproduces the amplitude of the decrease of the viscosity and the U shape of the experimental curve. From this process ending by the two polynomial functions for the maximum volume fraction versus F_{CI} , we obtain a maximum volume fraction of 0.87 around $F_{CI} = 0.3$ if we start from the pure CC suspension or $\Phi_{max} = 0.82$ if we start from the pure CI suspension, explaining that the two curves of Fig. 9a do not merge. These values of Φ_{max} can be compared to the maximum packing fraction: $\Phi_{RCP} + (1 - \Phi_{RCP})\Phi_{RCP} \sim 0.87$ for a bidisperse suspension of spheres in the large aspect ratio limit (Furnas 1931) (Dörr et al. 2013). Of course, our system composed of two polydisperse suspensions with furthermore the irregular shape of the CC particles is far from a bidisperse suspension of spheres, and we must keep in mind that it is only a semi quantitative approach.

Since the ratio of the diameters is quite large (almost a factor of six), we can take the limit where the CI particles have no real diameter and are simply a part of the suspending medium. In this case, we can consider that we have a suspension of CaCO₃ particles at a volume fraction $\Phi_{CC} = V_{CC}/V_{tot}$ in a suspension made of CI particles in the liquid composed of the mixture ethylene glycol–water. This is the homogenization approach, used to predict the Bingham viscosity in Fig. 9b, that we develop in the next section in order to predict the rheology of a bidisperse suspension from the one of each of its components.

Homogenization model for the viscosity of bidisperse suspensions

We are going to use the homogenization approach for the rheology of suspensions as derived by Chateau et al. (2008) in the context of particles suspended in a non-Newtonian fluid and applied more recently to the case of a suspension of calcium carbonate containing a small proportion of millimetric size fibers (Sidaoui et al. 2020). This model can be applied to a bidisperse suspension if there is a large size difference between the two species of particles, so we can consider that the CC particles are suspended in an homogeneous medium having a viscosity $\eta(\Phi'_{CI})$ where Φ'_{CI} is the interstitial volume fraction of the CI particles in the suspending liquid: $\Phi'_{CI} = V_{CI}/(V_L + V_{CI})$, where V_L is the volume of the suspending liquid. The total volume fraction of particles being given by $\Phi = (V_{CI} + V_{CC})/V_{tot}$, we shall end up with the following:

$$\Phi'_{CI} = \frac{\Phi \cdot F_{CI}}{\Phi \cdot F_{CI} + 1 - \Phi} \quad \Phi_{CC} = \frac{V_{CC}}{V_{tot}} = F_{CC} \cdot \Phi \quad (4)$$

where F_{CI} is the iron fraction of solid: $F_{CI} = V_{CI}/(V_{CI} + V_{CC})$ already defined. The viscosity of the whole suspension is then given by as follows:

$$\eta(\Phi, F_{CI}) = \eta_m(\Phi'_{CI}) \eta_r(\Phi_{CC}) \quad (5)$$

where η_r is the relative viscosity of a suspension of CC particles in a Newtonian liquid and Φ'_{CI} the interstitial volume fraction of CI particles. We are looking for the rheological law $\dot{\gamma}(\sigma)$ of the bidisperse suspension from the rheological law $\dot{\gamma}_m(\sigma_m)$ applying to the suspension of pure iron at the volume fraction Φ'_{CI} . The important point is that the stress σ_m is the one in the matrix of CI particles when a stress σ is applied to the whole suspension. For the sake of completeness, we have put in appendix the derivation of the relation between the stress and the shear rate in the matrix relatively to the stress and the shear rate in the whole suspension (Chateau et al. 2008):

$$\sigma_m = \sigma / \sqrt{(1 - \Phi_{CC}) \cdot \eta_r(\Phi_{CC})} \quad \text{and} \quad \dot{\gamma}_m = \sqrt{\frac{\eta_r(\Phi_{CC})}{1 - \Phi_{CC}}} \dot{\gamma} \quad (6)$$

So we need to do a measurement of the rheogram $\dot{\gamma}_m(\sigma_m)$ of a suspension of iron at the right volume fraction: Φ'_{CI} corresponding to the fraction F_{CI} and the total volume fraction Φ (cf. Equation (4)) and also of a suspension of pure calcium carbonate at the volume fraction Φ_{CC} in order to use the correspondence between the applied stress and the stress in the iron matrix (cf. Equation (6)).

Note that from Eq. (6), we have the following:

$$\frac{\sigma}{\dot{\gamma}} = \frac{\sigma_m}{\dot{\gamma}_m} \eta_r(\Phi_{CC}) \quad (7)$$

If the suspension of CI particles is Newtonian, which is practically true below the DST transition, we recover Eq. (5) with η_m the Newtonian viscosity of the suspension of CI particles. Before trying to apply this Newtonian approach to predict the variation of the Bingham viscosity with F_{CI} , at $\Phi = 0.705$, let us look at the whole experimental curves for high values of F_{CI} .

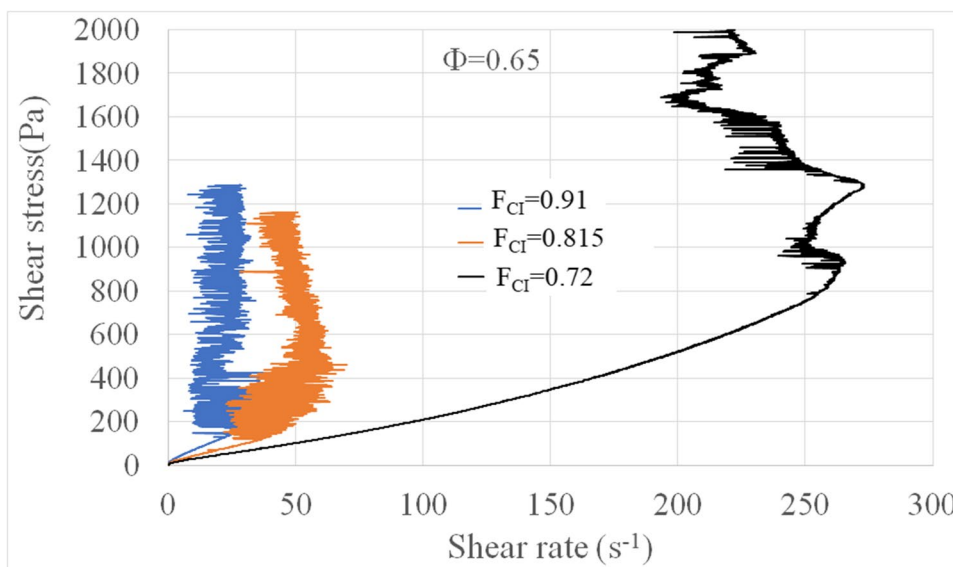
We have reported in Fig. 10 the stress versus shear rates curves for a total volume fraction $\Phi = 0.65$ and three high values of F_{CI} namely $F_{CI} = 0.91, 0.815,$ and 0.72 . To avoid expulsion at high shear rate, we have used cylindrical Couette geometry. For the three solid fractions of iron, we have a DST transition corresponding to the point of zero slope of $d\dot{\gamma}/d\sigma$. The viscosity increases when F_{CI} tends towards unity as already seen for the total volume fraction $\Phi = 0.705$. Again, we note that the critical stress σ_c is much higher for $F_{CI} = 0.72$ than for $F_{CI} = 0.815$ or 0.91 .

From Eq. (4), the corresponding volume fractions of the interstitial suspension of iron particles are respectively $\Phi'_{CI} = 0.628, 0.601,$ and 0.568 , and the apparent volume fraction of CC particles is respectively $\Phi_{CC} = 0.06, 0.121,$ and 0.182 . These values are reported in Table 2 as well as those of the relative viscosity of the pure suspension of CC particles: $\eta_r(\Phi_{CC})$. The viscosity of the suspending fluid (mixture water-ethylene glycol) was $\eta_0 = 0.012$ Pa.s at 20°C .

In Fig. 11a–c, we have reported in blue the experimental curves of Fig. 10 at $\Phi = 0.65$. The curves in black are the ones obtained for pure CI particles at the corresponding interstitial volume fractions $\Phi'_{CI} = 0.628, 0.602,$ and 0.572 , where we did not represent the fluctuating part for the clarity of the figure. Last, the red ones are the predictions using the correcting factors of Eq. (6). In this aim, we obtain the function $\dot{\gamma}_m(\sigma_m)$ from the inversion of the axes of the black curve with the help of a smoothing and of an interpolation function; then, we replace σ_m by σ using the correcting factor of Eq. (6), and we multiply by the second correcting factor to pass from $\dot{\gamma}_m(\sigma)$ to $\dot{\gamma}(\sigma)$.

We see that in the three cases, it does not work since the theoretical curves are well below the experimental ones. We can easily understand why because here, before the DST transition, the suspension is almost Newtonian, at least for $F_{CI} = 0.91$ and $F_{CI} = 0.815$, and the Bingham viscosity of the suspension is given by Eq. (5): $\eta(\Phi) = \eta_m(\Phi'_{CI}) \eta_r(\Phi_{CC})$. The ratio of the experimental value to the theoretical one is shown in Table 2, and we see that in the three cases, the use of the homogeneous approach strongly underestimates the viscosity of the mixture. In this range of viscosity (of a few Pa.s) and shear rate, the reproducibility is good, and the uncertainty on the viscosity is lower than $\pm 3\%$. Note that for $F_{CI} = 0.72$, the suspension is shear thickening, and we have taken for $\eta(\Phi)$ the Bingham viscosity for $\dot{\gamma} < 50 \text{ s}^{-1}$. In any

Fig. 10 Shear stress versus shear rate in cylindrical Couette geometry; total volume fraction, $\Phi=0.65$, and CI volume percentage of solid, $F_{CI}=0.91$, $F_{CI}=0.815$, and $F_{CI}=0.72$



event, as there is no DST transition in the pure iron suspension (Fig. 11c), the use of Eqs. (5)–(6) could never give a DST transition as the one shown by the blue curve. We can also notice that, in this theory for the Newtonian case before the transition, the ratio of the slope of the theoretical curve to the one of the pure suspension is just the relative viscosity of a suspension of the pure CC particles: $\eta_r(\Phi_{CC})$ given in Table 2. For instance, in the case $F_{CI}=0.91$, we should have $\eta_r(\Phi_{CC})=1.92$ instead of the experimental value of 1.15 to get the agreement between theory and experiment. One reason of this failure could be that there is some overlap between the two size distributions, but the volume of small CC particles which overlap with large CI particles is only 0.3% of the total volume of CC particles.

Another reason could be the increase of the interstitial density of the CI particles due to the presence of a depleted shell of CI particles at the surface of the large CC particles. This phenomenon was previously described (Madraki et al. 2018) in the case of a suspension of Cornstarch particles with larger PMMA particles where they observed that increasing the part of the large particles for the same internal volume fraction of small particles (in our case Φ'_{CI}) was triggering a DST transition.

To get an estimation of this excluded volume effect, we call Φ_{sh} the volume fraction of iron particles in a shell of thickness $d_{CI}=2 a_{CI}$ and $\Phi_{sh}=V_{CI-sh}/V_{sh}$ the volume fraction of CI particles inside this shell. The new volume fraction of iron particles in the domain outside this excluded volume is now: $\Phi''_{CI}=(V_{CI}-\Phi_{sh} V_{sh})/(V_{tot}-V_{ex})$ where $V_{ex}=V_{cc}+V_{sh}$ or with previously defined quantities:

$$\Phi''_{CI} = \frac{1-\Phi_{sh}f_s \left[\frac{1}{f_{CI}} - 1 \right]}{\frac{1}{f_{CI}} - f_s \left[\frac{1}{f_{CI}} - 1 \right]} = \frac{\Phi'_{CI}(1-\Phi_{cc}) - \Phi_{sh}f_s\Phi_{cc}}{1-\Phi_{cc}(1+f_s)} \quad \text{with } f_s = \frac{V_{sh}}{V_{cc}} = \frac{(a_{cc}+d_{CI})^3 - a_{cc}^3}{a_{cc}^3} \tag{8}$$

The volume fraction Φ_{sh} of the iron particles inside the shell is an unknown. One approach is to consider that the particles are reduced to their center of mass (Madraki et al. 2018); in that case, there is an excluded volume of thickness a_{CI} instead of d_{CI} and $\Phi_{sh}=0$ in Eq. (7). We can rather consider that we have a layer of thickness d_{CI} and take Φ_{sh} as a parameter. Taking $\Phi_{sh}=0.52$, the homogeneous approach is now predicting the right order of magnitude for the viscosity of the three bidisperse suspensions (cf. Table 2) at $\Phi=0.65$.

In Fig. 9a, we have shown that the use of the maximum volume fraction inferred from numerical simulation of a bidisperse suspension of spheres was able to quite well reproduce the drop of viscosity of the mixture, especially for $F_{CI}>0.4$. We can also try to use the homogenization approach to predict the evolution of the viscosity with F_{CI} for $\Phi=0.705$ (Fig. 9b). The green squares in Fig. 9b are obtained with the use of Eq. (7), and the first point at $F_{CI}=0$ is just the experimental value. We see that it reproduces quite well the drop of viscosity up to $F_{CI}=0.4$ but after it overestimates the drop of viscosity and, above all, fails by an order of magnitude to predict the strong increase of viscosity above $F_{CI}=0.5$. Now, if we consider the existence of this depleted shell of CI particles—this time with $\Phi_{sh}=0.58$ instead of 0.52—we can recover the increase of viscosity (Fig. 9b, green solid line). It highlights the fundamental role of the organization of the small particles in a corona around the large ones for the DST of a bidisperse suspension. A volume fraction between 0.5 and 0.6 for Φ_{sh} is slightly above the one of a cubic network ($\Phi_{sh}=\pi/6$) and seems plausible, but only numerical simulations of a bidisperse suspension with the real geometries of the particles could give a correct estimation of the volume fraction inside this depleted shell. It is also worth noting that Eq. (8) only

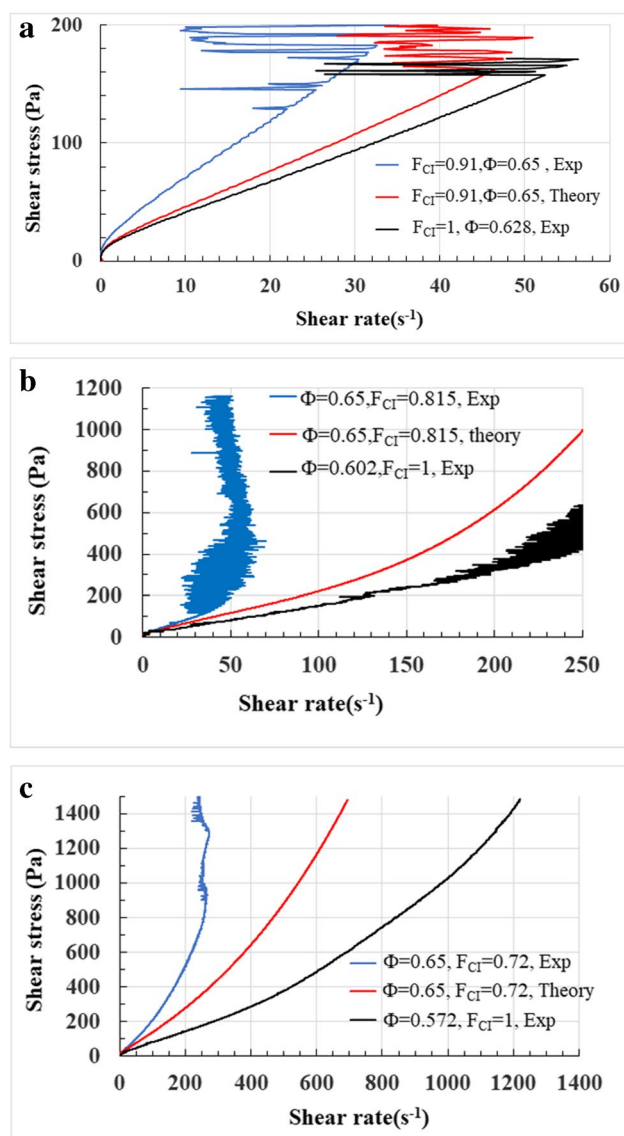


Fig. 11 Comparison between experiment (blue line) and homogenization theory (red line) for **a** $F_{CI}=0.91$, **b** $F_{CI}=0.815$, and **c** $F_{CI}=0.72$. The solid black line corresponds to the experiment for pure iron at the respective interstitial volume fraction: $\Phi'_{CI}=0.628$, $\Phi'_{CI}=0.602$, and $\Phi'_{CI}=0.572$

applies for $\Phi_{CC} < 1/(1+f_s)$ since the denominator of the second expression, which is the volume accessible to CI particles outside the surface shell and normalized by V_{tot} , must remain positive.

Synergetic effect of non-magnetic particles in the presence of a magnetic field

The effect of the magnetic field on the rheology of a magnetorheological suspension, usually made of CI particles in a suspending fluid, is to produce a yield stress whose value is

related to the attractive magnetic forces between the particles. Once the applied stress has overcome the magnetic stress, the suspension flows with a plastic viscosity which is quite insensitive to the yield stress. In Fig. 12, we have plotted three series of raw curves for values of fields: $H=0$ kA/m, $H=7.2$ kA/m, $H=14.4$ kA/m, and $H=21.5$ kA/m. The lowest one with dashed dotted lines correspond to a pure suspension of CI particles at a volume fraction $\Phi_{CI}=V_{CI}/V_{tot}=0.23$. We recover the increase of the yield stress with the field and a Bingham viscosity which remains approximately the same. The next two series of four dashed curves correspond to the same fields and to the same volume fraction $\Phi_{CI}=0.23$ of CI particles, but a part of the suspending fluid was replaced by CC particles corresponding either to $\Phi=0.73$ and $F_{CI}=0.32$ or to $\Phi=0.74$ and $F_{CI}=0.31$. In Fig. 13a, we have plotted the plastic viscosity defined as $\eta_p = \frac{\Phi_c - \tau_{yB}}{\dot{\gamma}_c}$ for $\Phi=0.73$ and 0.74 and by a Bingham fit between 100 and 200 s^{-1} for the pure CI suspension. One remarkable thing is that we have a very large increase of viscosity with the field in the presence of CC particles contrary to what happens for the same volume fraction of CI particles without CC particles. This is a manifestation of the synergetic effect since the presence of non-magnetic particles should not give a supplementary response in the presence of the magnetic field. When non-magnetizable spheres are included in the clusters formed by the application of the field, they enhance the interparticle forces on the compression axis as shown by numerical simulations (Wilson and Klingenberg 2017). Note that this behavior is opposite to the one observed by Zhang et al. (2008) where the DST transition was disappearing at high field and high fraction of CI particles. It could be due to the absence of a coating polymer on the surface of their CI particles that make them to aggregate in the presence of the field like in a conventional MR fluid.

The fact that we have a DST transition at zero field is also surprising because the corresponding interstitial volume fraction $\Phi'_{CI}=0.464$ is well below the volume fraction ($\Phi_{CI}=0.53$) corresponding to the onset of DST transition for the pure suspension of CI particles (Bossis et al. 2022). The same remark is true for the total volume fraction $\Phi=0.74$ with $F_{CI}=0.31$. A plausible explanation is that the onset of the DST transition for CI particles squeezed between CC particles is shifted towards lower volume fraction due to the perturbation of their piling in the presence of CC particles. This is related to the fact that, for the corresponding high volume fraction of CC particles ($\Phi_{CC} \sim 0.5$), the denominator of Eq. (8) is negative, meaning that the volume of the first shell of CI particles is already larger than the total volume devoted to CI particles; it will cause a smaller loose random packing than in the absence of boundaries. Coming back to the huge increase of the Bingham viscosity with the magnetic field, it is related to the combination of the particle

Fig. 12 Stress versus shear rate for three series of identical magnetic fields $H=0$ kA/m, 7.2 kA/m, 14.4 kA/m, and 21.5 kA/m. Dashed dotted lines: pure CI suspension at $\Phi=0.23$. Dashed lines: bidisperse suspensions: $\Phi=0.73$ and $F_{CI}=0.32$. Solid lines: $\Phi=0.74$ and $F_{CI}=0.31$. In the three suspensions, $\Phi_{CI} = V_{CI}/V_{tot} = 0.23$

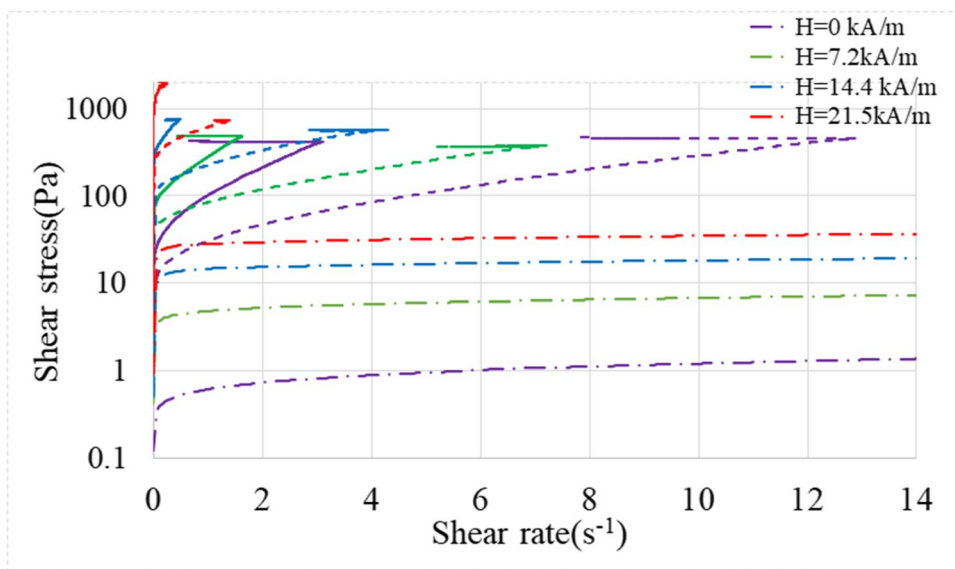
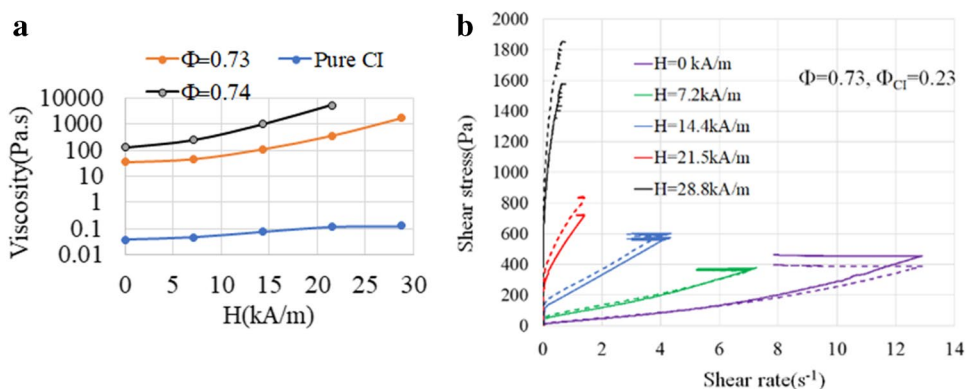


Fig. 13 **a** Plastic viscosity versus magnetic field for the three set of curves of Fig. 12. The volume fraction of CI particles, $\Phi_{CI}=0.23$, is the same for these three curves. **b** Same as Fig. 12 in linear scale for $\Phi=0.73$ and $\Phi_{CI}=0.23$. The dashed lines are the raw curves and the solid lines the corrected curves using Eq. (2)



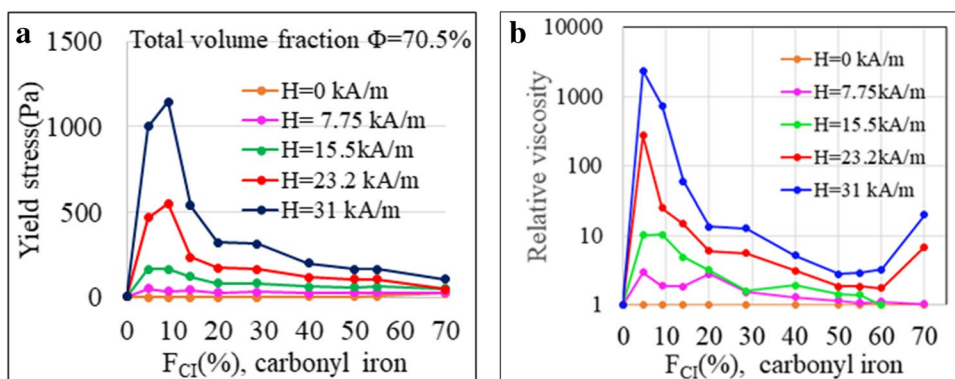
pressure induced by the high total volume fraction and the attractive force imposed by the application of the magnetic field. The magnetic pressure triggers the interpenetration of the brush like polymers coating both the CC and the CI particles. This enhanced friction between the polymers attached to different surfaces is likely responsible for the observed increase of viscosity with the magnetic field and finally for the DST transition when the shearing forces are large enough to sweep the polymer out of the surfaces. We also observe that the suspension is shear thickening at low field but becomes shear thinning for the two highest fields. This is evidenced in Fig. 13b where we have plotted both the raw curves and the ones corrected with Eq. (2). When the corrected curve (solid curve) is below the raw one and diverges more and more, it means that the suspension is shear thinning. For $H=14.4$ kA/m, the curves are parallel, and we have a Newtonian behavior whereas the two lowest ones are slightly shear thickening.

We have seen the synergetic effect of the non-magnetic particles on the change of viscosity and, to a less extent of

yield stress, in the presence of a magnetic field at an intermediate fraction of CI particles: $F_{CI}=31-32\%$. In Fig. 14a–b, we have plotted the evolution of the relative viscosity $\eta_B(H)/\eta_B(H=0)$ and of the Bingham yield stress τ_{yB} versus the fraction of CI particles for different magnetic fields.

In the absence of iron particles ($F_{CI}=0$), the Bingham yield stress is small ($\tau_y = 3.4$ Pa) and, of course, does not depend on the magnetic field. In the graph of Fig. 14b, we have plotted the Bingham viscosity divided by the one at zero field which is the one of Fig. 9a. Both for the yield stress and the relative viscosity we see that there is a huge increase at a small value of F_{CI} , around $F_{CI}=5\%$ and that, on the contrary, for high values of F_{CI} , this increase does not exist for the yield stress or is much more moderate with the viscosity. This is quite counter intuitive since we have more iron particles and less CC particles, and these are the iron particles which are sensitive to the magnetic field. Note that here we are dealing with the part of the rheogram which is below the DST transition. One explanation of this observation is that, under the magnetic field, a small quantity of

Fig. 14 **a** Bingham yield stress versus solid volume fraction of CI particles. Total volume fraction: $\Phi = 70.5\%$. **b** Relative viscosity $\eta_B(H)/\eta_B(H=0)$ versus solid volume fraction of CI particles. Total volume fraction $\Phi = 70.5\%$



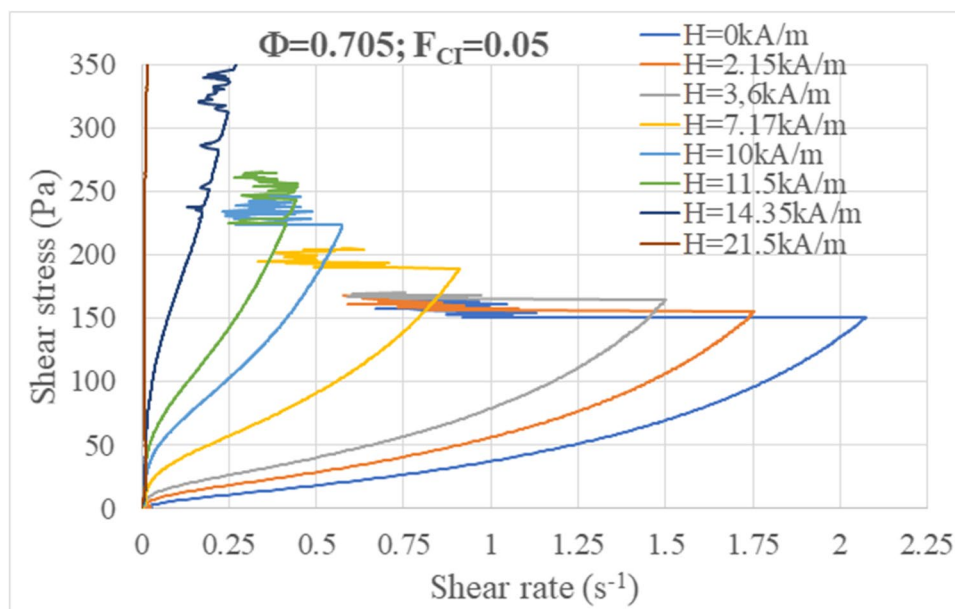
iron particles between CC particles can more easily form elongated structures which are, like fibers, very efficient to increase the viscosity and the yield stress due to their large effective volume fraction (Powell 1991). Furthermore, the internal magnetic field inside these needle-like aggregates is much higher than inside spherical ones due to the absence of local demagnetizing field (Bossis et al. 1997) which increases the internal cohesion of these linear aggregates, whose rotation under the shear flow will be blocked by the presence of CC particles. More importantly, we have to take into account that, when the fraction of iron particles increases, the magnetic permeability, μ , of the suspension also increases. For instance, in our experimental range of field, the relative permeability of the suspension of CI particles is approximately linear with the volume fraction: $\mu_r = 1 + 8.46\Phi_{CI}$ (de Vicente et al. 2002). In the plate-plate geometry, the average field inside the suspension is $H_i = H/\mu_r$; here, H is the external applied field, and it is almost divided by a factor of 5 between $F_{CI} = 0.05$ and $F_{CI} = 0.7$. As the yield stress $\tau_y \propto H_i^{3/2}$ at low fields (Ginder et al. 1996), it would give a decrease of the yield stress by a factor of eleven between $\Phi = 0.05$ and $\Phi = 0.7$, and experimentally we have a decrease by a factor of nine. Furthermore, the structure of the aggregates becomes more and more isotropic when F_{CI} increases, which, on a local scale, also contributes to decrease the internal field in the aggregates themselves and the presence of CC particles, just contributes to introduce defects in the network of CI particles whose cohesion is due to short range forces induced by the magnetic field. Thus, the effect of the demagnetizing field in plate-plate geometry can explain why the Bingham yield stress is decreasing with the increase of F_{CI} . This qualitative explanation is based on the hypothesis that the presence of nonmagnetic particles is as efficient as magnetic ones to transmit the magnetic stress so that the yield stress should not depend too much on F_{CI} except through the change of permeability. Also, the decrease of the maximum volume fraction with F_{CI} can play a role in the decrease of the field induced yield stress. This will likely play a similar role for the Bingham viscosity, although, to our knowledge, there

is no theoretical model for the evolution of the Bingham viscosity with the magnetic field. Actually, it is often supposed that the only effect of the magnetic field is to produce a yield stress which is the stress necessary to break the aggregates built by the attractive magnetic forces, but once the flow has started, the particles become free to move as in the absence of field. In other words, the Bingham viscosity is not changed by the application of the field. It is more or less true at low to intermediate volume fraction, but not at all at high volume fraction since the absence of free space between the particles combined to the attractive magnetic forces obliges the particles to remain in close contact and modifies the interpenetration length between the coating polymer layers. The higher is the field the more interpenetration we have, and the higher will be the Bingham viscosity. Nevertheless, we see that, unlike the yield stress, above $F_{CI} = 0.5$, we have a plateau followed by a clear increase of the viscosity at $F_{CI} = 0.7$. The cause which could counterbalance the decrease of the internal field is the one we have already described for $\Phi = 0.65$ (cf. Table 2), that is to say, the increase of the interstitial volume fraction of CI particles due to a lower concentration, Φ_{sh} , of the layer of CI particles on the surface of calcium carbonate particles.

In any event, the fact that both the yield stress and the viscosity increase a lot with the magnetic field whereas the fraction of CI particles is low is an interesting observation for the applications, since it allows to decrease the sedimentation effect and the irreversible aggregation of CI particles when the suspension remains at rest.

We have plotted in Fig. 15 the evolution with the magnetic field of the rheograms obtained at the optimum fraction $F_{CI} = 5\%$ and total volume fraction $\Phi = 0.705$. We better see on this graph the huge increase of viscosity produced by small magnetic fields (note that 1 Tesla corresponds to $H = 800\text{kA/m}$). For instance, the low shear rate viscosity is 36 Pa.s at zero field and 22,000 Pa.s at a field $H = 21.5\text{kA/m}$. In order to better understand the cause of this huge increase, let us see what is the prediction of the homogenization model in the presence of a magnetic field. If we apply Eq. (7), we can write:

Fig. 15 Evolution of the rheology with the magnetic field for a solid volume fraction of magnetic particles: $F_{CI}=5\%$ and a total volume fraction of solid $\Phi=0.705$



$$\eta(\Phi, H) = \eta_m(\Phi'_{CI}, H) \eta_r(\Phi_{CC}) \quad (9)$$

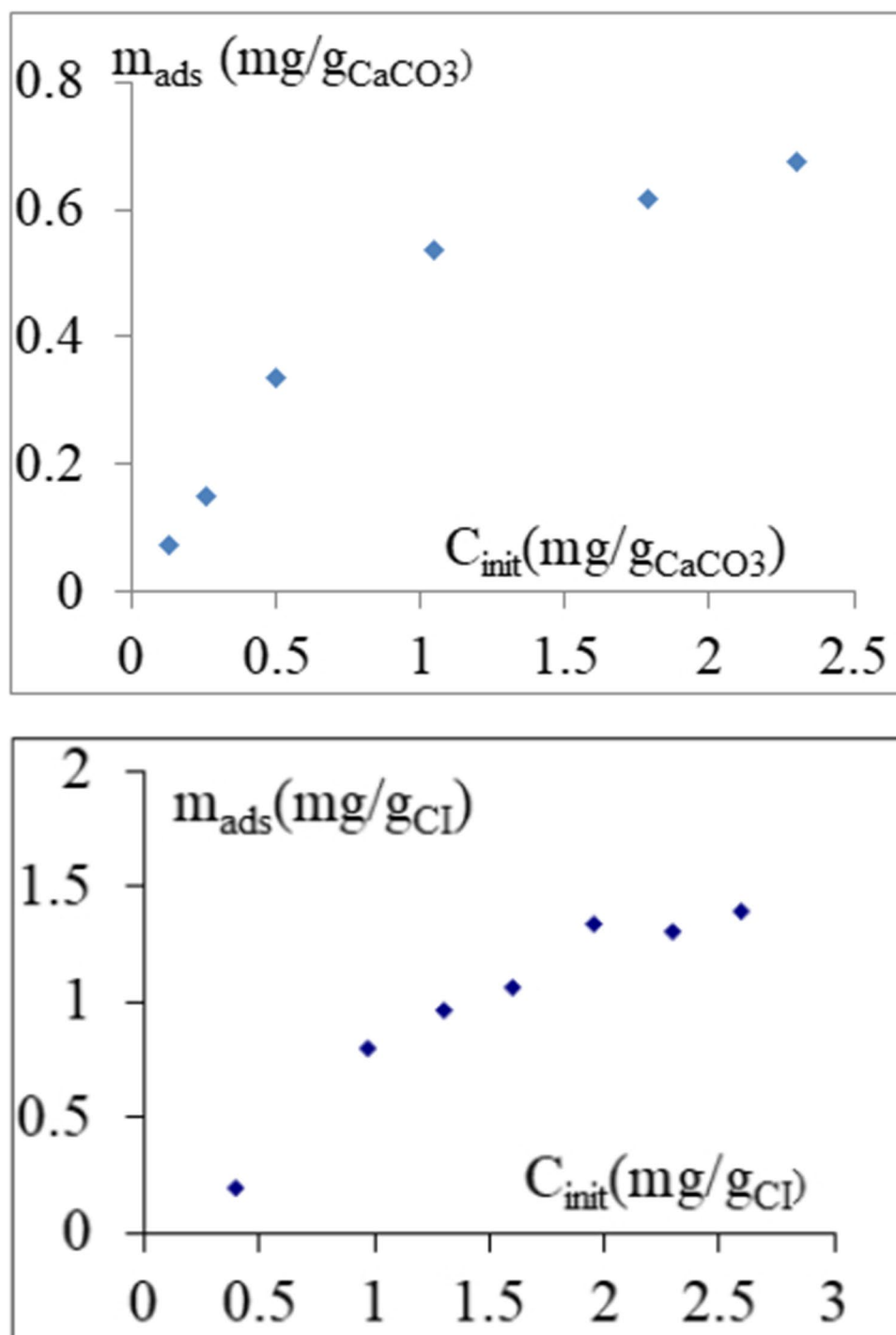
In Eq. (9), η_m is the viscosity of the suspension of CI particles at the interstitial volume fraction which, for $F_{CI}=5\%$ and $\Phi=0.705$, is equal to: $\Phi'_{CI} = 11\%$. On the other hand we have $\Phi_{CC}=0.67$ and $\eta_r(\Phi_{CC}) = 2203$. The Bingham viscosity of the pure iron suspension at $\Phi'_{CI} = 11\%$ increases from 0.017 Pa.s at zero field to 0.082 Pa.s at $H=21.5$ kA/m. The application of Eq. (9) gives $\eta(\Phi, H) = 37.4$ Pa.s at $H=0$ and 181 Pa.s for $H=21.5$ kA/m. Experimentally from the curves in Fig. 15, we get $\eta_B = 36$ Pa.s at $H=0$ and $\eta_B = 22,000$ Pa.s at $H=21.5$ kA/m. The first prediction in the absence of field is in the uncertainty range, as it was noted in Fig. 9b, but it is two orders of magnitude smaller than the experiment at $H=21.5$ kA/m. Once again, this huge disagreement with the homogeneous model caused by the application of the field likely comes from the chain formation of CI particles in the gaps between CC particles whose compression by the local shear rate between CC particles can induce a large interpenetration between the brush polymers and consequently an important increase of viscosity. A second observation, similar to the one made on Fig. 13b is that, before the transition, the suspension is shear thickening at low field but becomes shear thinning for the highest fields. In the frame of the Wyart-Cates theory, the shear thickening before the DST transition is related to the progressive formation of frictional contacts, but if it was the case here, we should expect that, increasing the field, it would produce more frictional contacts and then would increase the shear thickening. We propose that the observed shear thickening is mainly due to an increase of the interpenetration zone between the layers of polymer adsorbed on the particles which can increase the viscosity both through the formation

of transient aggregates of particles and through the increased dissipation in the interpenetration zone. When the field is increased, the thickness of this interpenetration zone will saturate due to the non-linear increase of osmotic and elastic repulsive forces. This saturation of the anisotropy of the pair distribution function will give a shear thinning behavior (Bossis and Brady 1989) until the applied stress overcomes the repulsive one and ejects the polymer from the surfaces of the particles, provoking the DST transition with dry friction between the particles. In this approach, the frictional contacts appear abruptly at a critical stress, whereas below the critical stress, the viscous behavior of the suspension is ruled by the interpenetration of the coating polymer layers. This interpretation was already developed in the case of pure CI suspensions (Bossis et al 2022).

Conclusion

In this work, we have seen first that the evolution of the Bingham viscosity of a mixture of carbonyl iron and calcium carbonate particles versus their relative volume fraction can be fairly reproduced from the dependence of the maximum volume fraction of a bidisperse suspension versus its composition. When the fraction F_{CI} of CI particles increases, keeping the same total solid volume fraction (here $\Phi=0.705$; cf. Figure 6), the critical stress of the DST transition strongly increases until the transition disappears for $0.2 < F_{CI} < 0.5$ and then decreases until at $F_{CI} > 0.72$, the suspension is jammed. At the same time, we observe that the shear thickening behavior before the DST transition is strong at intermediate values of F_{CI} but disappears at $F_{CI}=0.72$. The homogenization model, where the small particles are integrated to the

Fig. 16 **A** Adsorption isotherm of PPP44 on CaCO_3 particles in water at $T=20^\circ\text{C}$. **B** Adsorption isotherm of PPP44 on carbonyl iron particles in water at $T=20^\circ\text{C}$



suspending fluid, works well for $F_{\text{CI}} < 0.4$ but strongly underestimate the increase of viscosity above $F_{\text{CI}} = 0.6$. Introducing the volume fraction Φ_{sh} of CI particles in a corona around the CC particles allows to better recover the experimental behavior for $F_{\text{CI}} > 0.6$ (cf Fig. 9b) and at $\Phi = 0.65$ (cf. Table 2). We must nevertheless keep in mind that we have applied the homogenization model to polydisperse suspension instead of monodisperse ones, even if the overlap of the two size

distributions is very small (cf. Figure 2). The introduction of a depleted zone around the CC particles seems reasonable, due to geometrical constraints, and is supported by previous works (Vu et al. 2010) (Madraki et al. 2018), but other phenomena-like specific interactions between CC and CI particles, either hydrodynamic or deriving from their interaction energy, could also play a role. Numerical simulations would be useful to clarify what happen in this corona zone.

In the presence of a magnetic field, we highlight the synergistic effect of non-magnetic particles predicted by numerical simulations (Wilson and Klingenberg 2017) whose presence allows to transmit the forces induced by the magnetic forces throughout the measuring cell. Measuring the increase of yield stress and viscosity versus F_{CI} , we have obtained an unexpected result: Their increase was maximum for a small quantity of magnetic particles: $F_{CI} \sim 0.05$. This result was mainly explained by the fact that the internal field in the plate-plate geometry used in rheometry decreases when F_{CI} increases due to demagnetization effect. The effect of the magnetic field on the increase of viscosity for $F_{CI} > 0.6$ (cf. Figure 14b) could perhaps be explained by considering the volume fraction Φ_{sh} as in the absence of field, but already, in the presence of the magnetic field, the homogenization theory no longer works even at low values of F_{CI} . Another observation worth exploring is the fact that, increasing the field, the suspension can pass from shear thickening to shear thinning (cf. Figure 13b) which is contradictory with the scheme of an increase of the fraction of frictional contacts until the DST transition occurs (Wyart and Cates 2014). We think that, in the presence of a brush like coating of polymers, it is the increase of the interpenetration zone of the coating polymer, and not a progressive increase of frictional contacts, which trigger the DST transition.

At last, we want to emphasize that using a matrix of large non-magnetic particles enclosing in its pores, the small CI particles should be an efficient way to reduce their sedimentation and their aggregation due to the gravitational pressure $\rho \cdot g \cdot h$, since here, h would be of the order of the diameter of non-magnetic particles instead of the height of the cell. The reduction of the sedimentation allied with the maximum effect of the field at low volume fraction of CI particles should allow to considerably improve the area of application of MR suspensions.

Appendix 1. Homogenization theory

The homogenization approach starts from Eq. (5): for the viscosity of the bidisperse suspension:

$$\eta(\dot{\gamma}) = \eta_m(\sigma_m)\eta_r(\Phi_{cc}) \tag{10}$$

η_m is the viscosity of the matrix composed of the CI particles and of the liquid phase, η_r is the relative viscosity of a suspension of CC particles, and σ_m is the average stress in the matrix. The equality of dissipation calculated both in the macroscopic approach and the microscopic one reads

$$\sigma \dot{\gamma} V_{tot} = \int_{V_m} \sigma_m \dot{\gamma}_m \Rightarrow \frac{\sigma^2}{\eta(\dot{\gamma})} V_{tot} = \frac{\sigma_m^2}{\eta_m(\sigma)} V_m \tag{11}$$

where $V_m = V_{tot} - V_{cc}$ is the volume of the homogenous matrix. From (11), we have the following:

$$\frac{\sigma^2}{\eta_r(\Phi_{cc})} = \sigma_m^2 (1 - \Phi_{cc}) \tag{12}$$

Hence,

$$\sigma_m = \frac{\sigma}{\sqrt{(1 - \Phi_{cc})\eta_r(\Phi_{cc})}} \tag{13}$$

On the other hand, $\dot{\gamma}_m = \frac{\sigma_m}{\eta_m}$ and from (13) and (10), we get the following:

$$\dot{\gamma}_m = \gamma \sqrt{\frac{\eta_r(\Phi_{cc})}{1 - \Phi_{cc}}} \tag{14}$$

Appendix 2. Adsorption isotherm of PPP44 on iron and calcium carbonate particles

The measurement of the adsorption isotherm was realized with the method called total organic carbon (TOC). A suspension is made with a given mass of the superplasticizer molecule and of the particles (CI or CC particles). The suspension is rotated on a rotating bench for 12 h and then is centrifuged so as to recover only the suspending fluid. The TOC method works by combustion of the sample at a temperature of 680 °C. At this temperature, the organic or inorganic matter is transformed into CO₂, and an infrared cell makes it possible to measure it. From the final concentration of the superplasticizer in the suspending liquid, knowing the initial one, we can deduce the adsorbed mass versus the initial one. The results for carbonyl iron and calcium carbonate particles are presented in the following figures (Fig. 16).

The beginning of the adsorption plateau corresponds to the adsorption of a first layer of PPP44 on the surface of the particles, and we have chosen to work with a concentration of PPP44 of 2 mg/g of particles which in both cases well represent this adsorption of a monolayer.

Acknowledgements The authors want to thank the Centre National d’Etudes Spatiales (CNES, the French Space Agency) for having supported this research

Data availability Data can be available on request to the authors.

References

Abbott JR, Tetlow N, Graham AL et al (1991) Experimental observations of particle migration in concentrated suspensions: Couette flow. *J Rheol* 35:773–795

- Aruna MN, Rahman MR, Joladarashi S, Kumar H (2019) Influence of additives on the synthesis of carbonyl iron suspension on rheological and sedimentation properties of magnetorheological (MR) fluids. *Mater Res Express* 6:086105
- Ashtiani M, Hashemabadi SH, Ghaffari A (2015) A review on the magnetorheological fluid preparation and stabilization. *J Magn Magn Mater* 374:716–730
- Barnes HA, Hutton JF, Walters K (1989) *An introduction to rheology*. Elsevier
- Bossis G, Brady JF (1989) The rheology of Brownian suspensions. *J Chem Phys* 91:1866–1874
- Bossis G, Lemaire E, Volkova O, Clercx H (1997) Yield stress in magnetorheological and electrorheological fluids: a comparison between microscopic and macroscopic structural models. *J Rheol* 41:687–704. <https://doi.org/10.1122/1.550838>
- Bossis G, Grasselli Y, Meunier A, Volkova O (2016) Outstanding magnetorheological effect based on discontinuous shear thickening in the presence of a superplasticizer molecule. *Appl Phys Lett* 109:111902
- Bossis G, Boustingorry P, Grasselli Y et al (2017) Discontinuous shear thickening in the presence of polymers adsorbed on the surface of calcium carbonate particles. *Rheol Acta* 56:415–430
- Bossis G, Volkova O, Grasselli Y, Cifre A (2019) The role of volume fraction and additives on the rheology of suspensions of micron sized iron particles. *Front Mater*. <https://doi.org/10.3389/fmats.2019.00004>
- Bossis G, Grasselli Y, Volkova O (2022) Discontinuous shear thickening (DST) transition with spherical iron particles coated by adsorbed brush polymer. *Phys Fluids* 34:113317
- Bournonville B, Coussot P, Chateau X (2004) Modification du modèle de Farris pour la prise en compte des interactions géométriques d'un mélange polydispense de particules. *Rhéologie* 7:1–8
- Burguera EF, Love BJ, Sahul R et al (2008) A physical basis for stability in bimodal dispersions including micrometer-sized particles and nanoparticles using both linear and non-linear models to describe yield. *J Intell Mater Syst Struct* 19:1361–1367
- Cates ME, Haw MD, Holmes CB (2005) Dilatancy, jamming, and the physics of granulation. *J Phys: Condens Matter* 17:S2517
- Chae HS, Piao SH, Maity A, Choi HJ (2015) Additive role of attapulgite nanoclay on carbonyl iron-based magnetorheological suspension. *Colloid Polym Sci* 293:89–95
- Chateau X, Ovarlez G, Trung KL (2008) Homogenization approach to the behavior of suspensions of noncolloidal particles in yield stress fluids. *J Rheol* 52:489–506
- Chaudhuri A, Wang G, Wereley NM et al (2005) Substitution of micron by nanometer scale powders in magnetorheological fluids. *International Journal of Modern Physics* 19:1374–1380
- Chen K, Zhang WL, Shan L et al (2014) Magnetorheology of suspensions based on graphene oxide coated or added carbonyl iron microspheres and sunflower oil. *J Appl Phys* 116:153508
- Chin BD, Park JH, Kwon MH, Park OO (2001) Rheological properties and dispersion stability of magnetorheological (MR) suspensions. *Rheol Acta* 40:211–219
- Cho MS, Choi HJ, Jhon MS (2005) Shear stress analysis of a semiconducting polymer based electrorheological fluid system. *Polymer* 46:11484–11488
- Choi HJ, Jang IB, Lee JY et al (2005) Magnetorheology of synthesized core-shell structured nanoparticle. *IEEE Trans Magn* 41:3448–3450
- Choi JS, Park BJ, Cho MS, Choi HJ (2006) Preparation and magnetorheological characteristics of polymer coated carbonyl iron suspensions. *J Magn Magn Mater* 304:e374–e376
- Chow AW, Sinton SW, Iwamiya JH, Stephens TS (1994) Shear-induced particle migration in Couette and parallel-plate viscometers: NMR imaging and stress measurements. *Phys Fluids* 6:2561–2576
- Cvek M (2022) Constitutive models that exceed the fitting capabilities of the Herschel-Bulkley model: a case study for shear magnetorheology. *Mech Mater* 173:104445
- De Larrard F (1999) *Concrete mixture proportioning: a scientific approach*. CRC Press
- de Vicente J, Bossis G, Laci S, Guyot M (2002) Permeability measurements in cobalt ferrite and carbonyl iron powders and suspensions. *J Magn Magn Mater* 251:100–108. [https://doi.org/10.1016/S0304-8853\(02\)00484-5](https://doi.org/10.1016/S0304-8853(02)00484-5)
- Dörr A, Sadiki A, Mehdizadeh A (2013) A discrete model for the apparent viscosity of polydisperse suspensions including maximum packing fraction. *J Rheol* 57:743–765
- Egres RG, Wagner NJ (2005) The rheology and microstructure of acicular precipitated calcium carbonate colloidal suspensions through the shear thickening transition. *J Rheol* 49:719–746. <https://doi.org/10.1122/1.1895800>
- Ekwebelam C, See H (2009) Microstructural investigations of the yielding behaviour of bidisperse magnetorheological fluids. *Rheol Acta* 48:19–32
- Fall A, Lemaitre A, Bertrand F et al (2010) Shear thickening and migration in granular suspensions. *Phys Rev Lett* 105:268303
- Fall A, Bertrand F, Hautemayou D et al (2015) Macroscopic discontinuous shear thickening versus local shear jamming in cornstarch. *Phys Rev Lett* 114:098301
- Farr RS, Groot RD (2009) Close packing density of polydisperse hard spheres. *J Chem Phys* 131:244104
- Franks GV, Zhou Z, Duin NJ, Boger DV (2000) Effect of interparticle forces on shear thickening of oxide suspensions. *J Rheol* 44:759–779
- Fu Y, Yao J, Zhao H et al (2018) Bidisperse magnetic particles coated with gelatin and graphite oxide: magnetorheology, dispersion stability, and the nanoparticle-enhancing effect. *Nanomaterials* 8:714
- Furnas CC (1931) Grading aggregates-I.-Mathematical relations for beds of broken solids of maximum density. *Ind Eng Chem* 23:1052–1058
- Genç S, Phulé PP (2002) Rheological properties of magnetorheological fluids. *Smart Mater Struct* 11:140
- Ginder JM, Davis LC, Elie LD (1996) Rheology of magnetorheological fluids: models and measurements. *Int J Mod Phys B* 10:3293–3303
- Gondret P, Petit L (1997) Dynamic viscosity of macroscopic suspensions of bimodal sized solid spheres. *J Rheol* 41:1261–1274
- Graham AL, Altobelli SA, Fukushima E et al (1991) Note: NMR imaging of shear-induced diffusion and structure in concentrated suspensions undergoing Couette flow. *J Rheol* 35:191–201
- Guy BM, Ness C, Hermes M et al (2020) Testing the Wyart-Cates model for non-Brownian shear thickening using bidisperse suspensions. *Soft Matter* 16:229–237
- He D, Ekere NN (2001) Viscosity of concentrated noncolloidal bidisperse suspensions. *Rheol Acta* 40:591–598
- Iyengar VR, Foister RT (2002) Use of high surface area untreated fumed silica in MR fluid formulation. *US Patent* 6,451,219
- Jiang J, Hu G, Zhang Z et al (2015) Stick-slip behavior of magnetorheological fluids in simple linear shearing mode. *Rheol Acta* 9–10:859–867. <https://doi.org/10.1007/s00397-015-0877-4>
- Johnson DH, Vahedifard F, Jelinek B, Peters JF (2017) Micromechanical modeling of discontinuous shear thickening in granular media-fluid suspension. *J Rheol* 61:265–277
- Jun J-B, Uhm S-Y, Ryu J-H, Suh K-D (2005) Synthesis and characterization of monodisperse magnetic composite particles for magnetorheological fluid materials. *Colloids Surf, A* 260:157–164
- Kim JM, Lee SG, Kim C (2008) Numerical simulations of particle migration in suspension flows: frame-invariant formulation of curvature-induced migration. *J Nonnewton Fluid Mech* 150:162–176

- Klingenberg DJ, Zukoski CF (1990) Studies on the steady-shear behavior of electrorheological suspensions. *Langmuir* 6:15
- Laun HM, Bung R, Schmidt F (1991) Rheology of extremely shear thickening polymer dispersions (passively viscosity switching fluids). *J Rheol* 35:999–1034
- López-López MT, Kuzhir P, Lácis S et al (2006) Magnetorheology for suspensions of solid particles dispersed in ferrofluids. *J Phys: Condens Matter* 18:S2803
- López-López MT, Kuzhir P, Bossis G, Mingalyov P (2008) Preparation of well-dispersed magnetorheological fluids and effect of dispersion on their magnetorheological properties. *Rheol Acta* 47:787–796. <https://doi.org/10.1007/s00397-008-0271-6>
- López-López MT, Zubarev AY, Bossis G (2010) Repulsive force between two attractive dipoles, mediated by nanoparticles inside a ferrofluid. *Soft Matter* 6:4346–4349
- Madraki Y, Ovarlez G, Hormozi S (2018) Transition from continuous to discontinuous shear thickening: an excluded-volume effect. *Phys Rev Lett* 121:108001
- Mari R, Seto R, Morris JF, Denn MM (2014) Shear thickening, frictionless and frictional rheologies in non-Brownian suspensions. *J Rheol* 58:1693–1724. <https://doi.org/10.1122/1.4890747>
- Merhi D, Lemaire E, Bossis G, Moukalled F (2005) Particle migration in a concentrated suspension flowing between rotating parallel plates: investigation of diffusion flux coefficients. *J Rheol* 49:1429–1448
- Morillas JR, de Vicente J (2020) Magnetorheology: a review. *Soft Matter* 16:9614–9642
- Morini R (2013) Rhéologie de suspensions concentrées de carbonate de calcium en présence de fluidifiant. PhD Thesis, Université Nice HAL Id: tel-00950039. <https://theses.hal.science/tel-00950039>
- Morris JF, Brady JF (1998) Pressure-driven flow of a suspension: Buoyancy effects. *Int J Multiph Flow* 24:105–130. [https://doi.org/10.1016/S0301-9322\(97\)00035-9](https://doi.org/10.1016/S0301-9322(97)00035-9)
- Neuville M, Bossis G, Persello J et al (2012) Rheology of a gypsum suspension in the presence of different superplasticizers. *J Rheol* 56:435–451
- Ngatu GT, Wereley NM (2007) Viscometric and sedimentation characterization of bidisperse magnetorheological fluids. *IEEE Trans Magn* 43:2474–2476
- Pednekar S, Chun J, Morris JF (2018) Bidisperse and polydisperse suspension rheology at large solid fraction. *J Rheol* 62:513–526
- Pesche R, Bossis G, Meunier A (1998) Numerical simulation of particle segregation in a bidisperse suspension. Third International Conference on Multiphase Flow - ICMF'98, Lyon, 8–12 June 1998
- Pierce R, Choi Y-T, Wereley NM (2022) The effect of mesocarbon microbeads on magnetorheological fluid behavior. *J Intell Mater Syst Struct* 33:619–628
- Poslinski AJ, Ryan ME, Gupta RK et al (1988) Rheological behavior of filled polymeric systems II. The effect of a bimodal size distribution of particulates. *J Rheol* 32:751–771
- Powell RL (1991) Rheology of suspensions of rodlike particles. *J Stat Phys* 62:1073–1094
- Probst RF, Sengun MZ, Tseng T-C (1994) Bimodal model of concentrated suspension viscosity for distributed particle sizes. *J Rheol* 38:811–829
- Roupeck J, Michal L, Strecker Z et al (2021) Influence of clay-based additive on sedimentation stability of magnetorheological fluid. *Smart Mater Struct* 30:027001
- Seto R, Mari R, Morris JF, Denn MM (2013) Discontinuous shear thickening of frictional hard-sphere suspensions. *Phys Rev Lett* 111:218301
- Shah K, Oh J-S, Choi S-B, Upadhyay RV (2013) Plate-like iron particles based bidisperse magnetorheological fluid. *J Appl Phys* 114:213904
- Shaully A, Wachs A, Nir A (1998) Shear-induced particle migration in a polydisperse concentrated suspension. *J Rheol* 42:1329–1348
- Sidaoui N, Arenas Fernandez P, Bossis G et al (2020) Discontinuous shear thickening in concentrated mixtures of isotropic-shaped and rod-like particles tested through mixer type rheometry. *J Rheol* 64:817–836
- Singh A, Mari R, Denn MM, Morris JF (2018) A constitutive model for simple shear of dense frictional suspensions. *J Rheol* 62:457–468. <https://doi.org/10.1122/1.4999237>
- Tian Y, Jiang J, Meng Y, Wen S (2010) A shear thickening phenomenon in magnetic field controlled-dipolar suspensions. *Appl Phys Lett* 97:151904
- Ulicny JC, Snively KS, Golden MA, Klingenberg DJ (2010) Enhancing magnetorheology with nonmagnetizable particles. *Appl Phys Lett* 96:231903. <https://doi.org/10.1063/1.3431608>
- Van Ewijk GA, Vroege GJ, Philipse AP (1999) Convenient preparation methods for magnetic colloids. *J Magn Magn Mater* 201:31–33
- Viota JL, Durán JDG, González-Caballero F, Delgado AV (2007) Magnetic properties of extremely bimodal magnetite suspensions. *J Magn Magn Mater* 314:80–86
- Viota JL, Durán JDG, Delgado AV (2009) Study of the magnetorheology of aqueous suspensions of extremely bimodal magnetite particles. *Eur Phys J E* 29:87–94. <https://doi.org/10.1140/epje/i2009-10453-3>
- Vu T-S, Ovarlez G, Chateau X (2010) Macroscopic behavior of bidisperse suspensions of noncolloidal particles in yield stress fluids. *J Rheol* 54:815–833
- Wereley NM, Chaudhuri A, Yoo J-H et al (2006) Bidisperse magnetorheological fluids using Fe particles at nanometer and micron scale. *J Intell Mater Syst Struct* 17:393–401
- Wilson BT, Klingenberg DJ (2017) A jamming-like mechanism of yield-stress increase caused by addition of nonmagnetizable particles to magnetorheological suspensions. *J Rheol* 61:601–611
- Wu J, Pei L, Xuan S et al (2016) Particle size dependent rheological property in magnetic fluid. *J Magn Magn Mater* 408:18–25
- Wyart M, Cates ME (2014) Discontinuous shear thickening without inertia in dense non-Brownian suspensions. *Phys Rev Lett* 112:098302
- Zhang X, Li W, Gong XL (2008) Study on magnetorheological shear thickening fluid. *Smart Mater Struct* 17:015051

Publisher's note Springer Nature remains neutral with regard to jurisdictional claims in published maps and institutional affiliations.

Springer Nature or its licensor (e.g. a society or other partner) holds exclusive rights to this article under a publishing agreement with the author(s) or other rightsholder(s); author self-archiving of the accepted manuscript version of this article is solely governed by the terms of such publishing agreement and applicable law.